nature medicine

LETTERS

https://doi.org/10.1038/s41591-020-0926-0

Check for updates

A single-cell landscape of high-grade serous ovarian cancer

Benjamin Izar[1,2,3,4,5,14,15], Itay Tirosh[6,15], Elizabeth H. Stover[1,15], Isaac Wakiro[1], Michael S. Cuoco[3], Idan Alter[6], Christopher Rodman[3], Rachel Leeson[1], Mei-Ju Su[1,5], Parin Shah[1], Marcin Iwanicki[7], Sarah R. Walker[8], Abhay Kanodia[1], Johannes C. Melms[1], Shaolin Mei[5], Jia-Ren Lin[5], Caroline B. M. Porter[3], Michal Slyper[3], Julia Waldman[3], Livnat Jerby-Arnon[3], Orr Ashenberg[3], Titus J. Brinker[9], Caitlin Mills[5], Meri Rogava[5], Sébastien Vigneau[1,2], Peter K. Sorger[5], Levi A. Garraway[10], Panagiotis A. Konstantinopoulos[1], Joyce F. Liu[1], Ursula Matulonis[1], Bruce E. Johnson[1,2], Orit Rozenblatt-Rosen[3], Asaf Rotem[1,2,3,16] and Aviv Regev[3,11,12,13,16] ✉

Malignant abdominal fluid (ascites) frequently develops in women with advanced high-grade serous ovarian cancer (HGSOC) and is associated with drug resistance and a poor prognosis[1]. To comprehensively characterize the HGSOC ascites ecosystem, we used single-cell RNA sequencing to profile ~11,000 cells from 22 ascites specimens from 11 patients with HGSOC. We found significant inter-patient variability in the composition and functional programs of ascites cells, including immunomodulatory fibroblast sub-populations and dichotomous macrophage populations. We found that the previously described immunoreactive and mesenchymal subtypes of HGSOC, which have prognostic implications, reflect the abundance of immune infiltrates and fibroblasts rather than distinct subsets of malignant cells[2]. Malignant cell variability was partly explained by heterogeneous copy number alteration patterns or expression of a stemness program. Malignant cells shared expression of inflammatory programs that were largely recapitulated in single-cell RNA sequencing of ~35,000 cells from additionally collected samples, including three ascites, two primary HGSOC tumors and three patient ascites-derived xenograft models. Inhibition of the JAK/STAT pathway, which was expressed in both malignant cells and cancer-associated fibroblasts, had potent anti-tumor activity in primary short-term cultures and patient-derived xenograft models. Our work contributes to resolving the HSGOC landscape[3–5] and provides a resource for the development of novel therapeutic approaches.

Despite recent therapeutic advances, recurrent ovarian cancer is incurable and portends a poor prognosis with a median survival of approximately 1 year[6]. Intra-tumor heterogeneity of ovarian cancer cells and associated non-malignant cells is an important factor in driving treatment resistance, but remains poorly understood. Genomic analysis of high-grade serous ovarian cancer (HGSOC)—the most common and aggressive histological subtype—revealed *TP53* mutations, defects in homologous recombination DNA repair and extensive copy number aberrations in most tumors[2], and classified HGSOC into four transcriptional subtypes with distinct prognoses[2,7]. Ascites—comprised of a diverse collection of cell types—is present in one-third of patients with ovarian cancer at the time of diagnosis, and frequently occurs in patients with chemotherapy-resistant disease[8]. Here, we study ascites samples from patients with HGSOC, primary tumors and patient-derived xenograft (PDX) models by single-cell RNA sequencing (scRNA-seq), to resolve the expression profiles of diverse cancer, immune and stromal cells, and their interactions, each of which may contribute to disease development and treatment resistance[9–12].

We collected scRNA-seq data from three HGSOC cohorts totaling 35,957 high-quality cell profiles from a set of 22 ascites samples from 11 patients and a validation set (gathered separately) of three additional ascites samples and two primary tumors (Supplementary Table 1), collected through a translational workflow[9,13]. Together, this data compendium spans four treatment-naive, two on-treatment during initial chemotherapy, 18 on-treatment during disease recurrence, and two post-neoadjuvant chemotherapy specimens that reflect the substantial, real-life diversity among patients with HGSOC. We used three complementary profiling strategies (Fig. 1a, Extended Data Fig. 1a and Supplementary Table 1). First, to obtain a broad view of the different cell types in the ascites ecosystem, we analyzed eight specimens (partly depleted of CD45$^+$ immune cells; Methods) from six patients using massively parallel droplet scRNA-seq (cohort 1) (Methods). Second, because even after CD45$^+$ cell depletion, droplet-based profiling had a relatively low proportion of malignant cells (7.9%; see below), we complemented it by isolating 1,297 viable malignant EPCAM$^+$CD24$^+$ cells, which identify cancer cells with high sensitivity and specificity[14], from 14 ascites specimens from six individuals by fluorophore-activated

[1]Department of Medical Oncology, Dana-Farber Cancer Institute, Boston, MA, USA. [2]Center for Cancer Genomics, Dana-Farber Cancer Institute, Boston, MA, USA. [3]Klarman Cell Observatory, Broad Institute of MIT and Harvard, Cambridge, MA, USA. [4]Ludwig Center for Cancer Research at Harvard, Boston, MA, USA. [5]Laboratory for Systems Pharmacology, Harvard Medical School, Boston, MA, USA. [6]Department of Molecular Cell Biology, Weizmann Institute of Science, Rehovot, Israel. [7]Chemistry and Chemical Biology, Stevens Institute of Technology, Hoboken, NJ, USA. [8]Molecular, Cellular, and Biomedical Sciences, College of Life Sciences and Agriculture, University of New Hampshire, Durham, NH, USA. [9]German Cancer Research Center, Heidelberg, Germany. [10]Genentech, San Francisco, CA, USA. [11]Department of Biology, Massachusetts Institute of Technology, Cambridge, MA, USA. [12]Ludwig Center for Cancer Research at MIT, Boston, MA, USA. [13]Howard Hughes Medical Institute, Chevy Chase, MD, USA. [14]Present address: Columbia University Medical Center, Columbia Center for Translational Immunology, New York, NY, USA. [15]These authors contributed equally: Benjamin Izar, Itay Tirosh, Elizabeth H. Stover. [16]These authors jointly supervised this work: Asaf Rotem, Aviv Regev. ✉e-mail: aregev@broadinstitute.org

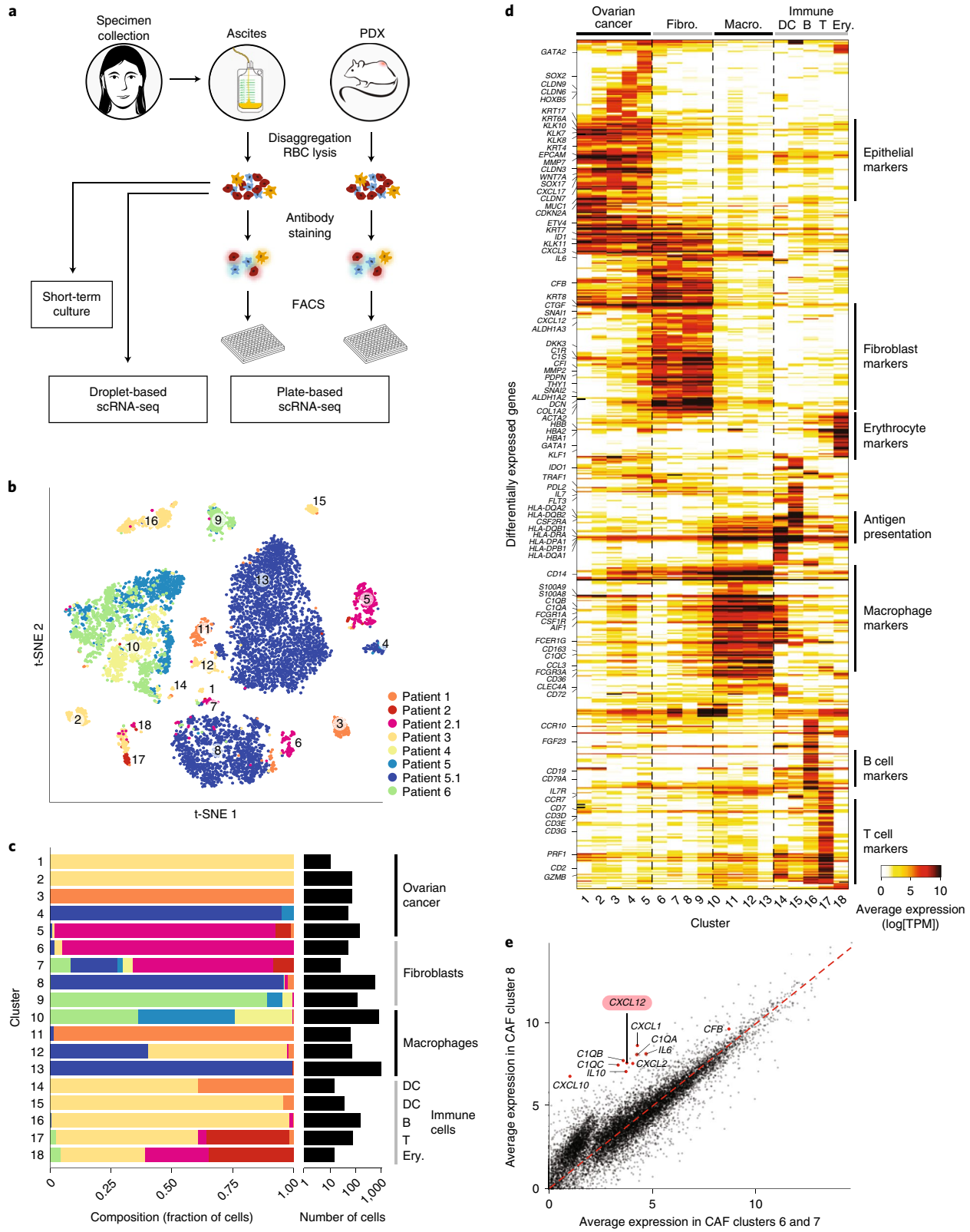

Fig. 1 | Charting the ovarian cancer ascites landscape by scRNA-seq. a, Overview of sample collection and the profiling strategy. RBC, red blood cell. **b**,**c**, Malignant and non-malignant cell clusters in patient ascites by droplet-based scRNA-seq. **b**, t-SNE of 9,609 droplet-based scRNA-seq profiles from eight samples, colored by sample of origin. Numbers indicate unsupervised assignment to 18 clusters. **c**, Fraction of cells (*x* axis) from each sample (color code as in **b**) in each cluster (*y* axis). Clusters are labeled (right) by their post-hoc annotation based on differentially expressed genes (as in **d**). DC, dendritic cells; ery., erythrocytes. **d**, Differentially expressed genes. The average expression ($\log_2$[TPM + 1]; color bar) of the top 30 genes (rows) that are differentially expressed in each cluster (columns) is shown. Genes are ordered by hierarchical clustering. Fibro., fibroblasts; macro., macrophages. **e**, An inflammatory subset of CAFs. Comparison of the average expression ($\log_2$[TPM + 1]) of each gene in CAF cluster 8 (*y* axis) versus CAF clusters 6 and 7 (*x* axis). Red points indicate immunomodulatory genes.

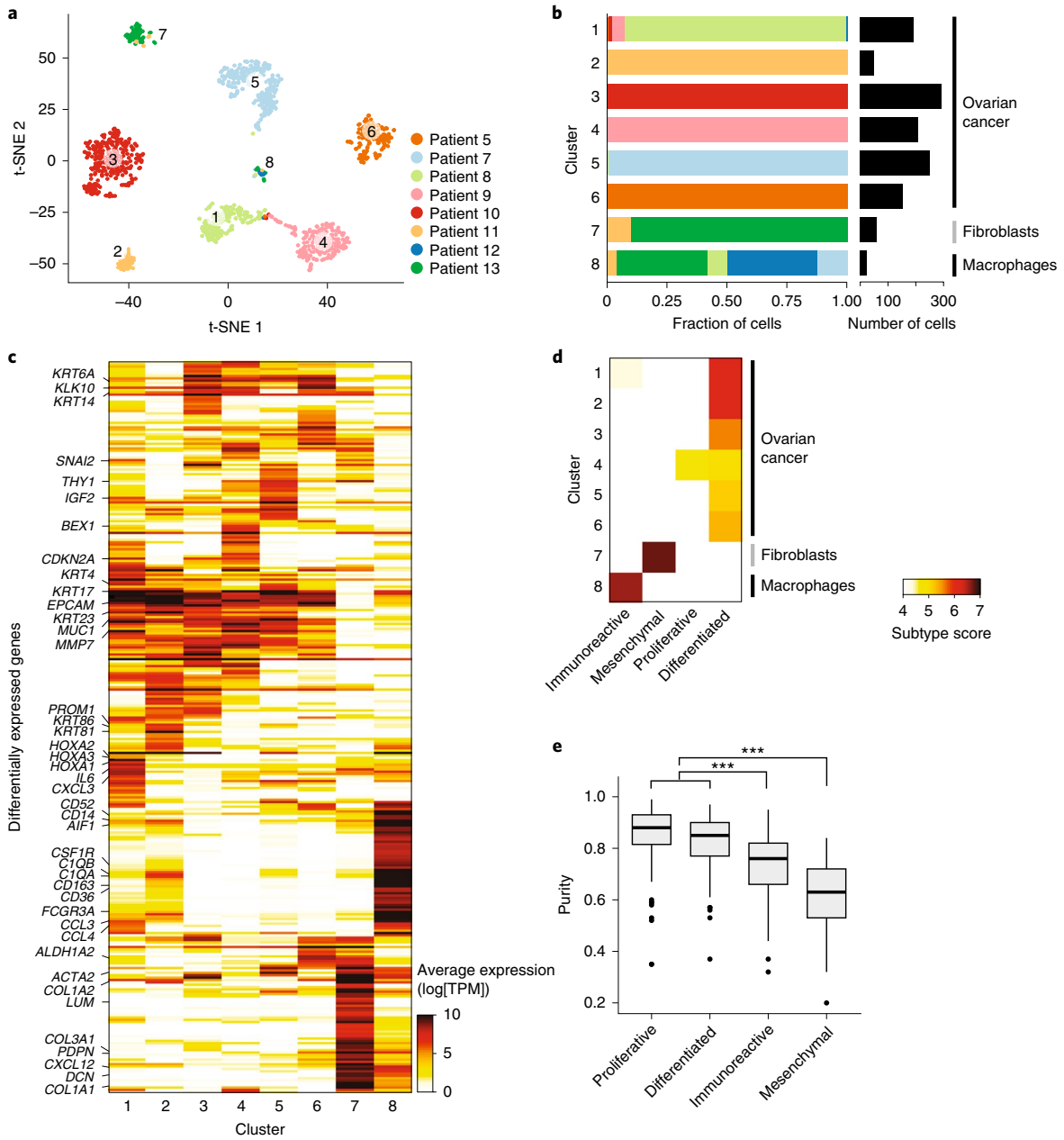

Fig. 2 | Malignant and non-malignant cell expression profiles help to identify the cellular basis of TCGA subtypes. a,**b**, Malignant cell clusters are enriched in patient ascites by FACS and plate-based scRNA-seq. **a**, t-SNE of 1,297 single-cell profiles from 14 ascites samples profiled by plate-based scRNA-seq, colored by patient. Numbers indicate unsupervised assignment to eight clusters. **b**, Fraction of cells (*x* axis) from each sample (color code as in **a**) in each cluster (*y* axis). Clusters are labeled (right) by their post-hoc annotation based on differentially expressed genes (as in **c**). **c**, Differentially expressed genes. Average expression ($\log_2$[TPM + 1]; color bar) of the top 30 genes (rows) that are differentially expressed in each cluster (columns). Genes are ordered by hierarchical clustering. **d**, The immunoreactive and mesenchymal subtypes reflect macrophages and fibroblast components. Subtype score (color bar), based on the average expression of subtype-specific genes (Methods) of each cluster (rows) for each of four TCGA subtypes (columns). **e**, Immunoreactive and mesenchymal TCGA subtypes have lower overall purity than differentiated and proliferative ones. The distribution of a purity estimate value (*y* axis; ABSOLUTE[39]; Methods) for TCGA ovarian cancer tumors ($n = 282$) in each subtype (*x* axis) is shown. Horizontal bars show mean values, box edges represent the interquartile range, whiskers show minimum and maximum values and dots represent outliers. ***$P < 10^{-10}$ (two-sided *t*-test).

cell sorting (FACS) into 96-well plates, followed by full-length scRNA-seq using a modified SMART-seq2 protocol[15,16] (cohort 2) (Methods). Third, as a validation set to examine the generalizability of our results, we assembled three additional ascites specimens (10,688 cells) and two primary tumors (14,505 cells) from the Human Tumor Atlas Pilot Project (HTAPP) (cohort 3)[17].

First, we used the droplet-based scRNA-seq (cohort 1) to identify and annotate 18 distinct cell clusters spanning epithelial cells (five clusters marked by *EPCAM*, as well as cytokeratin- and kallikrein-encoding genes), macrophages (four clusters marked by *CD14*, *AIF1*, *CSF1R* and *CD163*), cancer-associated fibroblasts (CAFs) (four clusters marked by *PDPN*, *DCN* and *THY1*), dendritic cells (two clusters marked by *CD1C*, *CD1E*, *CCR7* and *CD83*), B cells (*CD19* and *CD79A/B*), T cells (*CD2* and *CD3D/E/G*) and erythrocytes (*GATA1* and hemoglobin-encoding genes) (Fig. 1b–d, Extended Data Fig. 2a, Supplementary Table 2 and Methods).

Although we depleted CD45+ cells, immune cells remained the most abundant component, comprising on average 67% of the cells in each sample (ranging from 4–98%), highlighting a unique challenge of analyzing tumor cells from malignant effusions not usually encountered with solid tumor preparations[17]. The overall proportion of immune cells in each sample may reflect the differential efficiency of immune depletion (Methods), while other differences between samples may also be of biological origin (Fig. 1c). We examined whether different treatment histories explained differences in cellular ascites composition. Among cancer cells, there was marked inter-patient heterogeneity (Fig. 1b–d), which was not associated with previous treatment history (Extended Data Fig. 1b). Among CAFs and macrophages, expression profiles were similar across patients, indicating shared phenotypes, while the differences between patients were not clearly correlated with patients' treatment histories (Extended Data Fig. 1c). Determining whether expression patterns are linked to previous treatment exposures will require larger patient cohorts.

We examined the variation in macrophage and CAF subsets within and across patients. Macrophages and CAFs each comprised four clusters (Fig. 1c,d), driven by both inter- and intra-patient variability. While some clusters were comprised almost entirely of cells from a single patient, most had cells from multiple patients (Fig. 1c), including fibroblast clusters composed of cells from three or more patients.

Among CAFs, we identified distinct cell states, including sub-populations with expression of immune-related genes, such as complement factors (*C1QA/B/C* and *CFB*), chemokines (*CXCL1/2/10/12*) and cytokines (*IL6* and *IL10*) in clusters 8 and 9, compared with CAFs in clusters 6 and 7 (Fig. 1e and Extended Data Fig. 2b), suggesting a role as immunomodulatory CAFs[18,19]. This variation was also observed within a single patient: repeating the same analysis only with CAFs from patient sample 5.1 recapitulated CAF sub-populations based on the differential expression of 80 genes (Extended Data Fig. 2c). Among other cytokines expressed by these fibroblast subsets, CXCL12 and interleukin-6 (IL-6) activate JAK/STAT signaling across cancers[20].

Among macrophages, clusters 10 and 13 comprised the majority of cells. While most cells from cluster 13 derived from one patient sample (5.1), cluster 10 had cells from multiple patients. To examine intra-patient heterogeneity of macrophages, we focused on cells in cluster 10 from patient samples 6 and 5.0, each separating into two sub-populations (Extended Data Fig. 2d; groups 1 and 2) and characterized by consistent transcriptional programs. Group 1 cells co-expressed *HLA* genes encoding major histocompatibility complex (MHC) class II, *IFNGR1*, *CD1D*, *CD36* and *CD52*, whereas group 2 cells expressed complement factor components, cathepsin-encoding genes and *APO* genes (Extended Data Fig. 2e). Moreover, group 1 cells expressed several genes identified as markers for M1 macrophages (*IFNGR1*, *CD36*, *DDX5* and *MNDA*) and as suppressors of M2 differentiation (*C3AR1*), while group 2 cells expressed genes described in M2 macrophages, including those regulating M2 differentiation. While the M1/M2 dichotomy is currently being revised, this separation may indeed be associated with functional pro-/anti-tumor macrophage states. These findings generalized to samples with macrophages from all other patients (except patient sample 5.1) (Extended Data Fig. 2f).

We next sought to determine the inter- and intra-patient heterogeneity of malignant cells in HGSOC. To this end, we focused on the FACS-enriched, deeper-coverage, full-length scRNA-seq profiles (cohort 2), and identified eight clusters (Fig. 2a,b), including six of epithelial cells, one of CAFs (cluster 7) and one of macrophages (cluster 8) (Fig. 2b,c and Extended Data Fig. 3). We confirmed that the epithelial cells were malignant by inferring chromosomal copy number alterations (CNAs)[9] (Extended Data Fig. 4 and Methods). In contrast with macrophages and CAFs, the malignant cells clustered by their patient of origin (Fig. 2a,b), highlighting inter-individual variation. Some of this variation reflected the distinct CNA profile of each tumor (Extended Data Fig. 4), but additional genetic and epigenetic effects probably contributed to inter-patient variability among malignant cells.

Next, we asked whether inter-patient variability among malignant cells was consistent with the previously described The Cancer Genome Atlas (TCGA) subtypes—differentiated, proliferative, mesenchymal and immunoreactive—that have been derived from RNA expression profiling of bulk solid tumors from untreated patients with HGSOC and have been associated with varying prognoses[2]. We thus scored each cluster for the expression of TCGA-derived subtype signatures (Methods).

All six malignant cell clusters highly expressed the differentiated signature and only one (cluster 4) strongly expressed the proliferative signature (Fig. 2d and Extended Data Fig. 5), whereas the mesenchymal and immunoreactive signatures showed weak or no expression in cancer cell clusters, but were highly expressed by the CAF and macrophage clusters, respectively. Thus, the mesenchymal and immunoreactive subtypes may represent the intra-tumoral abundance of CAFs and macrophages, respectively. This is consistent with previous reports that TCGA tumors with these classifications had a significantly lower purity[21] (Fig. 2e), but the single-cell analysis showed that the immunoreactive and mesenchymal gene programs (such as those associated with epithelial–mesenchymal transition) were derived from the non-malignant immune cells and CAFs, respectively, as opposed to malignant cells. Thus, subtype classifications based on bulk RNA profiles probably predominantly reflect tumor ecosystem composition rather than cancer cell-derived HGSOC subtypes.

We then aimed to identify expression programs that vary among each patient's malignant cells. We used non-negative matrix factorization (NMF) and identified a total of 35 modules across malignant cells with coherently co-varying gene expression (Fig. 3a–c, Extended Data Fig. 6a,b and Supplementary Table 3). The modules spanned diverse functions, reflected by their top-scoring genes,

Fig. 3 | Inflammatory programs in malignant cells from patient ascites predict a role for JAK-STAT signaling. a–**c**, Intra-tumoral expression modules showing the relative expression (color bar; Methods) of the top 30 module-specific genes (rows) in each module (ordered by module; dashed horizontal lines), as defined by NMF (Methods) across all cancer cells (columns; ordered by hierarchical clustering) from patients 8 (**a**), 9 (**b**) and 10 (**c**). Selected genes are annotated. The top bar in **a** and **b** shows the sample times in three sequential samples from the same patient. **d**,**e**, Cell cycle and inflammatory/immune programs recur across patients. **d**, Number of top genes (color bar) shared between each pair of modules (rows and columns, ordered by hierarchical clustering). Top: module's patient of origin. **e**, Module membership in the top 30 (black) or 50 (gray) selected cell cycle (top) and immune-related (bottom) genes (rows) across all modules (columns), ordered as in **d**. IFN resp., interferon response. **f,** MHC class II-expressing cancer cells in situ. Representative immunofluorescence staining of HGSOC primary tissue, with staining for nuclei (blue), pan-keratin (green) and MHC class II (red). Scale bar: 20 μm. The overlay (right) shows co-expression of pan-keratin and MHC class II, indicating cancer cell-autonomous expression of MHC class II in a subset of cancer cells. **g**,**h**, Broad and high expression of JAK-STAT pathway components across malignant cells. **g**, Distribution of the average expression of genes (*x* axis, $\log_2$[TPM + 1]) for all detected genes (*y* axis). Red indicates the *STAT1/3* and *JAK1/STAT2* expression bins. **h**, Mean expression (*x* axis; $\log_2$[TPM + 1]) and percentage of expressing cells (*y* axis) of signaling genes. Key nodes of the JAK/STAT pathway are labeled. The line shows the LOWESS regression curve.

including cell cycle (for example, *CCNA2*, *CCNB2* and *AURKB*), inflammation (for example, *IL6*, *IL32*, *TNF* and *IFI6*) and stress or activation (for example, *HSPA5–7*, *ATF4*, *JUN* and *DDIT3*). One intriguing module consisted of prominent stemness[22] (*ALDH1A3* and *CD133/PROM1*) and mesenchymal markers (*FN1*, *ACTA2* and *MYL9*), and *AXL* and its only known ligand *GAS6*, which is

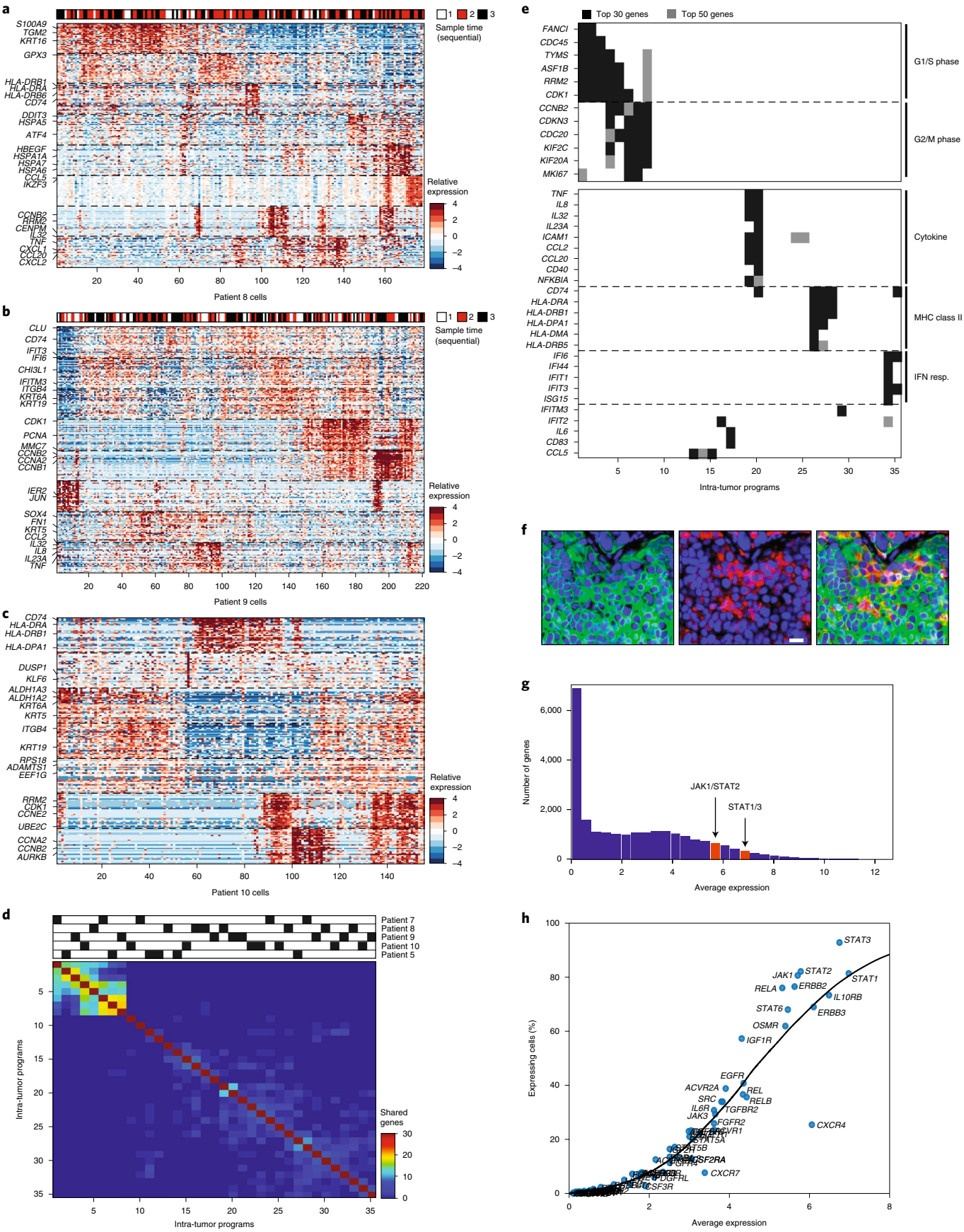

implicated in drug resistance[23] (Extended Data Fig. 6c-e); however, this program was unique to patient 7 and was not detected in cancer cells across the cohorts examined here (Extended Data Fig. 6c-f). Profiling of larger patient cohorts will be required to examine whether this is a recurrent stemness signature in HGSOC. Together, and in line with previous work[3,4,9–11], we found intra- and inter-individual heterogeneity of malignant and non-malignant cells, suggesting different functional sub-populations that contribute to shaping the HGSOC ecosystem.

To identify cancer cell programs shared across patients, we next compared the modules across different patients (Fig. 3d). As expected, there was strong overlap of cell cycle modules, indicating the presence of proliferating sub-populations of cells in all specimens. In addition, three programs dominated by immune- or inflammation-associated genes were shared among patients (Fig. 3d,e): an inflammatory cytokines module (for example, *IL6*, *TNF*, *IL8* and *IL32*), an MHC class II antigen presentation module (for example, *CD74* and *HLA-DRA*) and an interferon-response module (for example, *IFI6*, *IFIT1* and *ISG15*). These immune-related programs were also detected in cells from cohort 3, including three additional ascites samples and two primary tumors (Extended Data Fig. 6h–j). Cancer cell-intrinsic expression of MHC class II protein has recently been described in other epithelial cells[24,25], tumor-initiating cells[26] and cancers, such as melanoma[27], and can be associated with response to immunotherapies even in the absence of MHC class I expression[27]. We confirmed the expression of the MHC class II module in copy number variant-bearing malignant cells (Extended Data Fig. 6g) and showed by immunofluorescence staining of independent primary HGSOC tumors the presence of a sub-population of MHC class II-expressing cancer cells (among other cells that express MHC class II) (Fig. 3f).

Inflammatory cancer cell programs may be induced by the ascites microenvironment or reflect an endogenous property of the cancer cells. To evaluate these possibilities, we profiled 795 cells by scRNA-seq of three previously established PDX models (DF20, DF68 and DF101) (Methods) grown as subcutaneous tumors in immunocompromised animals[28] collected pre-, on and post-platinum therapy (Methods). Globally, PDX and patient cancer cells were as strongly correlated with each other (Pearson's $r = 0.819$ on average) as cancer cells of different PDX models ($r = 0.822$ on average) or cancer cells across patients (inter-patient comparison; $r = 0.882$ on average) (Extended Data Fig. 7a). Next, we identified 24 programs in the PDX models by NMF (Extended Data Fig. 7b-d and Supplementary Table 4) and compared them with those identified in patient ascites (Extended Data Fig. 7e,f).

Nine PDX modules were analogous to those from patient samples, including three reflecting cell cycle (PDX modules 1–3) and three interferon-response programs (PDX modules 6–8) (Extended Data Fig. 7f), highlighting this as the most significant similarity (apart from the cell cycle) between patterns of heterogeneity in patients and PDX models. The other two inflammation-related programs found in patients (cytokine and antigen presentation modules) were not detected in PDX models (Extended Data Fig. 7g), suggesting that their expression in cancer cells may depend on an intact immune system (mostly absent in nod *scid* gamma (NSG) mice) or other microenvironmental cues.

Multiple observations led us to consider the JAK/STAT pathway as a potential vulnerability. First, as described above, sub-populations of cancer cells highly expressed three immune-related programs that may be downstream from the JAK/STAT pathway. Second, cells in the ascites microenvironment, such as CAFs, highly expressed genes of secreted ligands (for example, *IL6* and *CXCL12*) that activate the JAK/STAT pathway. Third, analysis of a large set of signaling genes highlighted a particularly high and ubiquitous expression of JAK/STAT pathway components both in malignant and non-malignant cells (Fig. 3g,h and Extended Data Fig. 8a).

To determine the impact of JAK/STAT inhibition, we performed a drug screen using 15 compounds targeting different nodes of the pathway or its effectors, and platinum chemotherapies (Supplementary Table 5) in the HGSOC cell line OVCAR4, and identified JSI-124 (ref. [29]) as a potent inhibitor of cell viability (Fig. 4a and Extended Data Fig. 8b,c). JSI-124 showed anti-tumor activity at nanomolar doses in three different patient-derived cell culture models and additional HGSOC cell lines[30], while other drugs frequently used for the treatment of patients with HGSOC had little to no activity (Fig. 4b,c and Extended Data Fig. 9). JSI-124 also reduced the formation of three-dimensional clusters (spheroids) and their invasion through a mesothelial monolayer (modeling the abdominal peritoneum, which represents an important barrier for metastatic disease) (Fig. 4d–f and Supplementary Videos 1–4). In the PDX model DF20, which has substantial transcriptional similarity to patient ascites cancer cells (Extended Data Fig. 7a), early initiation of JSI-124 treatment (7 d after intraperitoneal or subcutaneous injection of tumor cells) abrogated the development of malignant ascites and tumor growth, respectively (Fig. 4g,i). Furthermore, JSI-124 significantly reduced disease burden in models where

Fig. 4 | JAK/STAT inhibition reduces viability, spheroid formation and invasion of HGSOC models ex vivo and in vitro. a, JSI-124 reduces cell viability in the OVCAR4 ovarian cancer cell line. Shown is the relative (mean) viability compared with the control in GILA (*y* axis), following 2 d of treatment of the OVCAR4 cell line with each of 14 inhibitors of the JAK/STAT pathway, as well as carboplatin and cisplatin (*x* axis). $^{**}P_{adj} = 0.0032$ for JSI-124 (one-way analysis of variance (ANOVA) with Holm–Bonferroni correction with Holm–Šídák extension). Error bars represent s.d. ($n = 3$). **b**, JSI-124, but not the other compounds routinely used for the treatment of ovarian cancer, reduces the mean viability of patient-derived ex vivo cultures. Shown is the percentage viability relative to DMSO-treated cells (*y* axis) in ex vivo cultures derived from patients 3, 5 and DF3291, each of which was treated for 48 h with increasing doses (*x* axis) of JSI-124, carboplatin, cisplatin, paclitaxel or olaparib. Error bars represent s.d. ($n = 4$). The results are representative of biological duplicates. **c**,**d**, JSI-124 leads to spheroid disintegration. **c**, Examples of light microscopy images of spheroids treated with the indicated compounds (representative of biological triplicates). **d**, Average number of spheroids (relative to DMSO-treated controls; *y* axis) formed with five established ovarian cancer cell lines (*x* axis) treated with two doses of JSI-124 or carboplatin. $^{*}P_{adj} < 0.05$ (one-way ANOVA with Holm–Bonferroni correction with Holm–Šídák extension). Error bars represent s.e.m. ($n = 3$). **e**,**f**, JSI-124 treatment reduces mesothelial clearance by patient-derived spheroids from patient-derived cultures and established cell lines. Shown are the levels of mesothelial clearance (*y* axis) by patient-derived cells (NACT8) treated with either JSI-124 (for 30 or 120 min) or DMSO (**e**), or by the ovarian cancer cell lines OVCAR8 and TYKNU, treated for 30 min (**f**). A total of 20 spheroid clusters were assessed per iteration. $^{**}P < 0.01$ (one-way ANOVA and post-hoc Tukey–Kramer test). The results are representative of two independent experiments with $n = 20$ spheroids per condition. Horizontal bars show mean values, box edges represent the interquartile range, and whiskers show minimum and maximum values. **g**–**j**, JSI-124 prevents tumor growth and eliminates established tumors in PDX models. Shown are the mean log[BLI signal] values (*y* axis) from PDX mice injected with DF20 tumor cells and treated with either vehicle (black) or JSI-124 (red) and monitored over time (*x* axis). Error bars represent s.e.m. ($n = 5$ mice per group). All statistical tests were two-sided *t*-test comparing mean ± s.d. values at day 15 of treatment. **g**, Mice were injected intraperitoneally (IP) and started treatment 1 week later for 14 d. $^{***}P < 0.0001$. **h**, Mice were injected IP, malignant ascites were allowed to form, and treatment started at 21 d and lasted another 14 d. $^{**}P = 0.002$. **i**, Mice were injected subcutaneously (SC) and started treatment 1 week later for 14 d. $^{***}P < 0.0001$. **j**, Mice were injected SC, tumors were allowed to form, and treatment started at 21 d and lasted another 14 d. $^{**}P = 0.0028$.

intraperitoneal ascites and subcutaneous tumors were grown for 21 d before treatment initiation (Fig. 4h,j). Together, these results suggest that JAK/STAT inhibition may be a potent therapeutic option for patients with HGSOC, through action on malignant cells, non-malignant cells or both.

Discussion

Our scRNA-seq study of malignant ascites from patients with advanced HGSOC reveals significant variability in cellular states and programs among malignant and non-malignant cells. Among non-malignant cells, we observed diversity among CAFs, with a subset expressing immunomodulatory programs, as recently proposed in other cancer types, such as pancreatic ductal adenocarcinoma[19], where inflammatory CAFs strongly express IL-6 and other cytokines and may promote tumor growth and drug resistance. Shared activation of the JAK/STAT pathway in cancer cells and CAFs suggests that paracrine (and/or autocrine) signaling via this pathway may contribute to the pathogenesis of malignant ascites and drug resistance, and provide one example of how cell-to-cell interactions shape the ascites ecosystem. Macrophage diversity primarily involved one major axis of variation driven by two gene programs: one including MHC class II, interferon-γ receptor 1 and

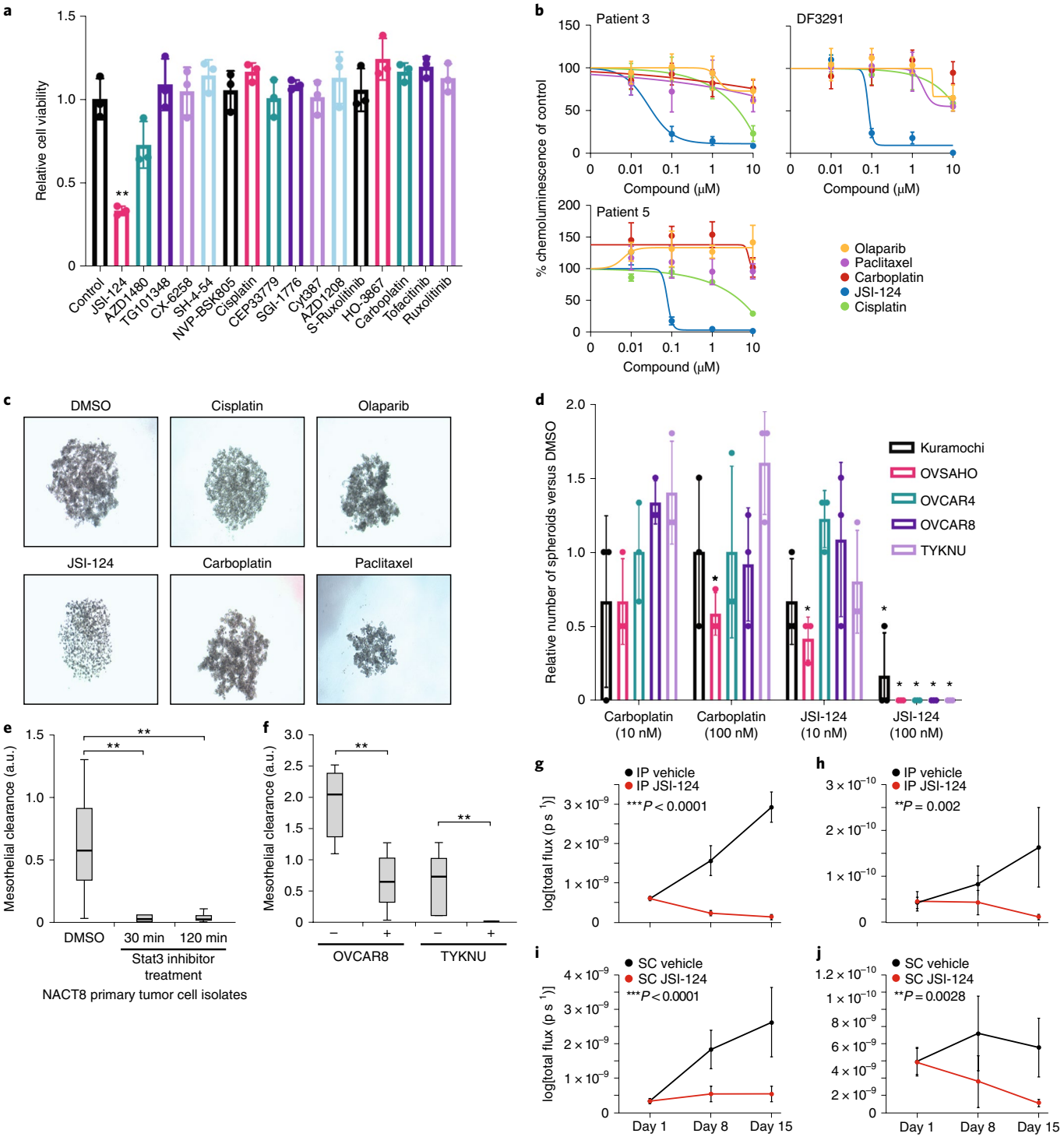

M1-associated genes, and the other by complement factors, suggesting that a balance of these phenotypes exists within the ascites ecosystem. Previous reports indicate that platinum therapy may further push this balance towards M2 macrophages by altering monocyte differentiation[31]. Such changes may occur rapidly, as indicated in a shift from M1-like to M2-like macrophage programs in one patient pair (5.0 and 5.1) examined pre-treatment and during treatment with platinum chemotherapy.

Variation across cancer cells was driven primarily by inter-patient variation, including CNA patterns, but additional subtler intra-patient variation was also present, such as a putative stemness program unique to a sub-population of cells in patient 7. Some of the intra-patient patterns of heterogeneity were consistent across multiple patients. For example, subsets of malignant cells expressing the MHC class II program were present in multiple patients and may be associated with an increased abundance of tumor-infiltrating lymphocytes, improved prognosis and response to immunotherapies[32]. MHC class II-expressing subsets were not identified in PDXs, suggesting that they may depend on immune cell interactions. An interferon-response and a cytokine program also co-varied across malignant cells in multiple patients. Thus, significant cellular and transcriptional forces within the ascites ecosystem (pro-tumorigenic or pro-immunogenic) may balance disease progression and responses to therapies. Therapeutically shifting this balance may be one avenue for reshaping the drug-resistant milieu.

Previous work focusing on intra-patient and intra-lesion genetic variability showed that development and response to therapy of primary tumors or metastatic lesions emerge as a result of co-evolution of malignant and non-malignant compartments[33,34]. Similarly, we hypothesize that interactions between CAFs and macrophages in the ascites ecosystem regulate or enhance cancer cell-autonomous programs. One example is the putative interaction between CAFs secreting IL-6 to stimulate JAK/STAT signaling in cancer cells, which is associated with poor prognosis and resistance to chemotherapies[35]. Consistently, JAK/STAT inhibition promoted anti-tumor activity in several pre-clinical models. Clinical trials, such as a phase I/II study using combination therapies with the JAK/STAT inhibitor ruxolitinib (NCT02713386) will help to clarify the role of such therapies in HGSOC.

HGSOC subtypes defined by TCGA have been associated with prognosis and drug response[2,36]. In our study, the vast majority of cancer cells across patients strongly expressed the differentiated subtype program, and a minority of cells from one patient also expressed the proliferative subtype program. In contrast, the mesenchymal and immunoreactive subtype programs were not expressed by cancer cells, but reflected programs expressed by CAFs and macrophages, respectively, and therefore represent tumor composition rather than salient cancer cell programs. While previous work could not evaluate the relative contribution of CAFs and cancer cells to the mesenchymal subtype (which also includes epithelial–mesenchymal transition genes), our results suggest that most, if not all, of this subtype can be explained by CAFs. This is consistent with findings in colorectal[37] and head and neck cancer[12]. Increased CAF infiltration may contribute to the low response rates to certain therapies, such as immune checkpoint inhibitors, whose efficacy is impacted by the tumor microenvironment[38].

Future studies should enhance our work in two main ways. First, profiling a larger number of patient samples would allow us to test for the generality of programs identified only in one patient (for example, the stemness program in patient 7) in our study. Second, single-cell profiling of well-stratified clinical cohorts, rather than the diverse patient population in our analysis (included to recapitulate true-to-life clinical heterogeneity), should enhance inter-patient comparisons and identify converging aspects of tumor biology and drug resistance, to improve our understanding of HGSOC.

Online content

Any methods, additional references, Nature Research reporting summaries, source data, extended data, supplementary information, acknowledgements, peer review information; details of author contributions and competing interests; and statements of data and code availability are available at https://doi.org/10.1038/s41591-020-0926-0.

Received: 1 July 2019; Accepted: 7 May 2020;
Published online: 22 June 2020

References

1. Matulonis, U. A. et al. Ovarian cancer. *Nat. Rev. Dis. Primers* **2**, 16061 (2016).
2. Cancer Genome Atlas Research Network Integrated genomic analyses of ovarian carcinoma. *Nature* **474**, 609–615 (2011).
3. Winterhoff, B. J. et al. Single cell sequencing reveals heterogeneity within ovarian cancer epithelium and cancer associated stromal cells. *Gynecol. Oncol.* **144**, 598–606 (2017).
4. Shih, A. J. et al. Identification of grade and origin specific cell populations in serous epithelial ovarian cancer by single cell RNA-seq. *PLoS ONE* **13**, e0206785 (2018).
5. Hu, Z. et al. The repertoire of serous ovarian cancer non-genetic heterogeneity revealed by single-cell sequencing of normal fallopian tube epithelial cells. *Cancer Cell* **37**, 226–242.e7 (2020).
6. Siegel, R. L., Miller, K. D. & Jemal, A. Cancer statistics, 2016. *CA Cancer J. Clin.* **66**, 7–30 (2016).
7. Patch, A.-M. et al. Whole-genome characterization of chemoresistant ovarian cancer. *Nature* **521**, 489–494 (2015).
8. Ahmed, N. & Stenvers, K. L. Getting to know ovarian cancer ascites: opportunities for targeted therapy-based translational research. *Front. Oncol.* **3**, 256 (2013).
9. Tirosh, I. et al. Dissecting the multicellular ecosystem of metastatic melanoma by single-cell RNA-seq. *Science* **352**, 189–196 (2016).
10. Tirosh, I. et al. Single-cell RNA-seq supports a developmental hierarchy in human oligodendroglioma. *Nature* **539**, 309–313 (2016).
11. Venteicher, A. S. et al. Decoupling genetics, lineages, and microenvironment in IDH-mutant gliomas by single-cell RNA-seq. *Science* **355**, eaai8478 (2017).
12. Puram, S. V. et al. Single-cell transcriptomic analysis of primary and metastatic tumor ecosystems in head and neck cancer. *Cell* **171**, 1611–1624.e24 (2017).
13. Izar, B. & Rotem, A. GILA, a replacement for the soft-agar assay that permits high-throughput drug and genetic screens for cellular transformation. *Curr. Protoc. Mol. Biol.* **116**, 28.8.1–28.8.12 (2016).
14. Peterson, V. M. et al. Ascites analysis by a microfluidic chip allows tumor-cell profiling. *Proc. Natl Acad. Sci. USA* **110**, E4978–E4986 (2013).
15. Picelli, S. et al. Smart-seq2 for sensitive full-length transcriptome profiling in single cells. *Nat. Methods* **10**, 1096–1098 (2013).
16. Trombetta, J. J. et al. Preparation of single-cell RNA-seq libraries for next generation sequencing. *Curr. Protoc. Mol. Biol.* **107**, 4.22.1–4.22.17 (2014).
17. Slyper, M. et al. A single-cell and single-nucleus RNA-Seq toolbox for fresh and frozen human tumors. *Nat. Med.* **26**, 792–802 (2020).
18. Cirri, P. & Chiarugi, P. Cancer associated fibroblasts: the dark side of the coin. *Am. J. Cancer Res.* **1**, 482–497 (2011).
19. Öhlund, D. et al. Distinct populations of inflammatory fibroblasts and myofibroblasts in pancreatic cancer. *J. Exp. Med.* **214**, 579–596 (2017).
20. Iliopoulos, D., Hirsch, H. A. & Struhl, K. An epigenetic switch involving NF-κB, Lin28, let-7 microRNA, and IL6 links inflammation to cell transformation. *Cell* **139**, 693–706 (2009).
21. Aran, D., Sirota, M. & Butte, A. J. Systematic pan-cancer analysis of tumour purity. *Nat. Commun.* **6**, 8971 (2015).
22. Silva, I. A. et al. Aldehyde dehydrogenase in combination with CD133 defines angiogenic ovarian cancer stem cells that portend poor patient survival. *Cancer Res.* **71**, 3991–4001 (2011).
23. Wu, X. et al. AXL kinase as a novel target for cancer therapy. *Oncotarget* **5**, 9546–9563 (2014).
24. Biton, M. et al. T helper cell cytokines modulate intestinal stem cell renewal and differentiation. *Cell* **175**, 1307–1320.e22 (2018).
25. Smillie, C. S. et al. Intra- and inter-cellular rewiring of the human colon during ulcerative colitis. *Cell* **178**, 714–730.e22 (2019).
26. Miao, Y. et al. Adaptive immune resistance emerges from tumor-initiating stem cells. *Cell* **177**, 1172–1186.e14 (2019).
27. Rodig, S. J. et al. MHC proteins confer differential sensitivity to CTLA-4 and PD-1 blockade in untreated metastatic melanoma. *Sci. Transl. Med.* **10**, eaar3342 (2018).
28. Liu, J. F. et al. Establishment of patient-derived tumor xenograft models of epithelial ovarian cancer for preclinical evaluation of novel therapeutics. *Clin. Cancer Res.* **23**, 1263–1273 (2016).

29. Blaskovich, M. A. et al. Discovery of JSI-124 (cucurbitacin I), a selective Janus kinase/signal transducer and activator of transcription 3 signaling pathway inhibitor with potent antitumor activity against human and murine cancer cells in mice. *Cancer Res.* **63**, 1270–1279 (2003).
30. Barretina, J. et al. The Cancer Cell Line Encyclopedia enables predictive modelling of anticancer drug sensitivity. *Nature* **483**, 603–607 (2012).
31. Dijkgraaf, E. M. et al. Chemotherapy alters monocyte differentiation to favor generation of cancer-supporting M2 macrophages in the tumor microenvironment. *Cancer Res.* **73**, 2480–2492 (2013).
32. Axelrod, M. L., Cook, R. S., Johnson, D. B. & Balko, J. M. Biological consequences of MHC-II expression by tumor cells in cancer. *Clin. Cancer Res.* **25**, 2392–2402 (2019).
33. Jiménez-Sánchez, A. et al. Heterogeneous tumor-immune microenvironments among differentially growing metastases in an ovarian cancer patient. *Cell* **170**, 927–938.e20 (2017).
34. Zhang, A. W. et al. Interfaces of malignant and immunologic clonal dynamics in ovarian cancer. *Cell* **173**, 1755–1769.e22 (2018).
35. Duan, Z. et al. Signal transducers and activators of transcription 3 pathway activation in drug-resistant ovarian cancer. *Clin. Cancer Res.* **12**, 5055–5063 (2006).
36. Kommoss, S. et al. Bevacizumab may differentially improve ovarian cancer outcome in patients with proliferative and mesenchymal molecular subtypes. *Clin. Cancer Res.* **23**, 3794–3801 (2017).
37. Calon, A. et al. Stromal gene expression defines poor-prognosis subtypes in colorectal cancer. *Nat. Genet.* **47**, 320–329 (2015).
38. Pitt, J. M. et al. Targeting the tumor microenvironment: removing obstruction to anticancer immune responses and immunotherapy. *Ann. Oncol.* **27**, 1482–1492 (2016).
39. Carter, S. L. et al. Absolute quantification of somatic DNA alterations in human cancer. *Nat. Biotechnol.* **30**, 413–421 (2012).

Methods

Collection of patient specimens. Specimens were collected from patients with ovarian cancer at Brigham and Women's Hospital and the Dana-Farber Cancer Institute under Institutional Review Board-approved protocols 02–051 and 11–104. Ascites fluid was drained by an interventional radiologist and transferred for further processing in closed-vacuum bottles. De-identified patient information, including their ovarian cancer histology, stage, treatment history and *BRCA1/2* mutation status, was collected.

Sample handling, flow cytometry and single-cell isolation. Immediately following drainage, malignant ascites were transported on ice, aliquoted into 50-ml conical tubes (BD Falcon) and spun for 5 min at 580*g* at 4 °C. The supernatant was aspirated and the remaining pellet was resuspended with 5 ml hypotonic lysis buffer ACK (Life Technologies) and incubated on ice for 5 min. Then, 20 ml phosphate-buffered saline (PBS) was used to quench the lysis buffer. Cell suspensions were pooled and pipetted into a new 50-ml conical tube through a 100-µm mesh and spun for 5 min at 580*g* at 4 °C. Hypotonic lysis was repeated until no visible red blood cell component was present, usually for a total of two or three times (for the plate-based approach). Following red blood cell lysis, the cell pellet was resuspended in PBS with 2% (vol/vol) fetal bovine serum (FBS). These cells were then used for both plate-based and droplet-based scRNA-seq. For plate-based scRNA-seq, cells were labeled with the following fluorophore-conjugated flow cytometry antibodies: live/dead stain with Calcein-AM (Life Technologies), 7-aminoactinomycin D (Life Technologies), CD45-FITC (VWR; 304006; clone HI30), EPCAM-PE (Miltenyi Biotec; 130-111-116; clone REA764) and CD24-PE/Cy7 (BioLegend; 311119; clone ML5). Cells were incubated for 30 min on ice in the dark. Cells were washed twice by resuspending with PBS with 2% (vol/vol) FBS and spun for 5 min at 580*g* at 4 °C. Flow cytometry and sorting were performed on a BD Biosciences cell sorter. Following doublet exclusion, calcein^{high}7AAD^{-}CD45^{-}EPCAM^{+}CD24^{+} single cells were sorted into 96-well microtiter plates (on a plate chiller) that were prepared with 10 µl cell lysis buffer (TCL + 1% β-mercaptoethanol). Following completion of cell sorting, plates were covered with aluminum lids, vortexed for 10 s, centrifuged for 2 min at 580*g* at 4 °C, and immediately placed on dry ice before storage at −80 °C.

Plate-based scRNA-seq. Plate-based scRNA-seq following FACS enrichment was used to strongly enrich for malignant cells. This approach complements efforts using the droplet-based method (below) where the non-malignant compartment makes up the vast majority of cells, but also includes a relatively small portion of cancer cells but with more shallow data. To balance both approaches, we used both to complement different types of analyses. For plate-based scRNA-seq, we performed whole-transcriptome amplification with a modified Smart-seq2 protocol, as described previously[15,16], with Maxima Reverse Transcriptase (Life Technologies) instead of Superscript II. Next, whole-transcriptome amplification products were cleaned with Agencourt XP DNA beads and 70% ethanol (Beckman Coulter), and Illumina sequencing libraries were prepared using Nextera XT (Illumina), as previously described[16]. The 96 samples of a multiwell plate were pooled, then cleaned with two 0.8× DNA SPRIs (Beckman Coulter). Library quality was assessed with a high-sensitivity DNA chip (Agilent) and quantified with a high-sensitivity dsDNA Quant Kit (Life Technologies). Barcoded single-cell transcriptome libraries were sequenced with 38-base pair paired-end reads on an Illumina NextSeq 500 instrument.

Droplet-based scRNA-seq. Single cells were isolated from patient-derived ascites as described above for all but one solid tumor, which was prepared for single-nucleus isolation as recently described[17]. Upon drainage of ascites, we immediately processed fresh specimens by removal of red blood cells using ACK lysis buffer, filtration and isolation of a single-cell suspension. Next, CD45^{+} cells were depleted using the MACS beads and columns, per the manufacturer's instructions (Miltenyi Biotec). While this approach led to only partial depletion of CD45^{+} immune cells (the main component of ascites), we avoided repeated bead-based depletion, because it results in RNA degradation and compromises subsequent scRNA-seq[17]. Next, cells were counted and resuspended in PBS supplemented with 0.04% BSA for loading for single-cell library construction on the 10× Genomics platform. Experiments were performed with the Chromium Single Cell 3′ Library & Gel Bead Kit v2 and Chromium Single Cell 3′ Chip Kit v2 according to the manufacturer's instructions in the Chromium Single Cell 3′ Reagents Kits V2 User Guide. Briefly, ~6,000 cells were loaded into each channel, then partitioned into gel beads in emulsion in the GemCode instrument, where cell lysis and barcoded reverse transcription of RNA occurred, followed by amplification, shearing and 5′ adaptor and sample index attachment. Barcoded single-cell transcriptome libraries were sequenced with 38 base pair paired-end reads on an Illumina NextSeq 500 instrument. The HTAPP cohort was processed and analyzed as recently described[17].

Cell culture. The HGSOC cell lines Kuramochi, Ovsaho, Ovcar4, Ovcar8 and Tyknu were provided by the Cancer Cell Line Encyclopedia project at the Broad Institute. All cell lines were cultured in RPMI 1640 Medium (Gibco), supplemented with 10% FBS and 1% penicillin/streptomycin (Invitrogen), and were maintained in an incubator at 37 °C and 5% CO_2. Sub-culturing of cell lines was done by detaching cells using 0.05% trypsin EDTA, quenching, washing and resuspending the cell pellet in fresh media.

In vitro and ex vivo drug sensitivity testing. The growth in ultra-low-attachment (GILA) assay[40] was used to assess the drug sensitivity of patient-derived cell lines and established cell lines. Five ovarian cancer cell lines (Kuramochi, Ovsaho, Ovcar4, Ovcar8 and Tyknu) were each plated at 5,000 cells per 100 µl AR-5 medium (ACL4 media with 5% FBS)[41] per well in both flat-bottomed high-attachment (Corning; 353072) and round-bottomed ultra-low-attachment (ULA) (Sigma–Aldrich; CLS7007-24EA) 96-well plates. For the initial screen with JAK/STAT pathway inhibitors, cells were treated with AZD1480 (AstraZeneca), NVP-BSK805 (Selleck Chemicals), TG101348 (STEMCELL Technologies), CX-6258 (Selleck Chemicals), CEP33779 (Selleck Chemicals), Ruxolitinib (Novartis), Tofacitinib (Pfizer), SGI-1776 (Sigma–Aldrich), Cyt387 (Selleck Chemicals), S-Ruxolitinib (Selleck Chemicals), AZD1208 (AstraZeneca), HO-3867 (Cayman Chemical), SH-4–54 (Selleck Chemicals), trametinib (GlaxoSmithKline), JSI-124 (Sigma–Aldrich), cisplatin (APP Pharmaceuticals) or carboplatin (Hospira) using 1 µM in both ULA and high-attachment plates. Cells were collected on day 0 (control) or after 48 h of treatment, covered with an aluminum lid, and flash frozen at −80 °C. Within 24 h of freezing, the cell viability of the samples was determined by CellTiter-Glo Luminescent Cell Viability Assay (CTG; Promega Corporation; G7572). The CTG reagent was thawed and diluted with 1× PBS in a 1:1 ratio before use. Plates were thawed and resuspended in equal volumes of CTG, then shaken on an orbital shaker at 100 r.p.m. for 2 min at room temperature to the mix contents and induce cell lysis. The plates were incubated at room temperature for 10 min to stabilize the luminescence signal. The cell culture and CTG reagent mixture was transferred to a white 96-well plate (Thermo Fisher Scientific; 07200722) and the luminescence signal was read on a 2103 EnVision Multilabel Plate Reader (PerkinElmer). Data analysis was performed using Excel and Prism.

Primary cell cultures were generated by removing red blood cells and depleting CD45^{+} cells using the MACS beads and columns, per the manufacturer's instructions (Miltenyi Biotec). Then, 5,000 cells per 100 µl AR-5 medium per well were plated in both high-attachment and ULA 96-well plates. For the GILA assay, 5,000 cells per well were seeded, maintained for 24 h and treated with either JSI-124 (Sigma–Aldrich), cisplatin (APP Pharmaceuticals), carboplatin (Hospira), olaparib (AstraZeneca) or paclitaxel (Life Technologies) at the indicated doses of 0.01 µM, 0.1 µM, 1 µM and 10 µM in both ULA and high-attachment plates. After three or five days of treatment, plates were covered with aluminum lids and flash frozen at −80 °C, followed by CTG assay as described above. Data analysis was performed using Excel and Prism.

Spheroid formation inhibition assay. Five ovarian cancer cell lines (Kuramochi, Ovsaho, Ovcar4, Ovcar8 and Tyknu) were plated in flat-bottomed ULA plates with either 0.1% DMSO, JSI-124 or carboplatin, at doses of 10 nM, 100 nM and 1 µM. After 48 and 72 h, spheroids with a diameter of >200 µm were counted using a CK40 Culture Microscope (Olympus America). The relative spheroid count was determined as a ratio of spheroids in the treatment conditions compared with DMSO-treated cells.

Culturing of patient-derived spheroids. Ovarian primary cells were frozen with 90% fetal bovine serum (FBS) and 10% DMSO at −80 °C and transferred to a liquid nitrogen tank for long-term storage. For spheroid assays, cells were thawed, washed in PBS, resuspended in AR-5 media and divided into flat-bottomed, ultra-low-attachment 6-well plates (Sigma–Aldrich; CLS3471-24EA) and maintained in an incubator at 37 °C and 5% CO_2 for 4 d. The media was replaced every 48 h. After 96 h, the cell suspension was passed through a 20-µm filter (Miltenyi Biotec; 130-101-812) to capture the spheroids larger than 20 µm in diameter. Reverse filtration was performed with AR-5 media to capture the spheroids that remained on the filter. The spheroids were collected and plated in ultra-low-attachment 6-well plates for short-term culture.

Mesothelial clearance assay. Primary ovarian cancer cells (NACT8) were cultured in a low-attachment 6-well plate for 96 h. The culture was treated with 10 µM JSI-124 or DMSO for 30 or 120 min. Spheroids were isolated by passing the suspension through a 20-µm filter. Reverse filtration was performed to collect spheroids larger than 20 µm into a 6-well plate. Cells were washed and spheroids were collected for the mesothelial clearance assay. A mesothelial cell monolayer was prepared by plating mesothelial cells on glass-bottomed dishes (MatTek Corporation) coated with 5 µg ml^{-1} fibronectin (Sigma–Aldrich). Cells were maintained in culture until confluent (~48 h after plating). Suspended NACT8 cell spheroids were collected and added to a confluent mesothelial monolayer expressing green fluorescent protein, allowed to attach for 30–60 min, then imaged for up to 16 h using a Nikon Ti-E inverted motorized widefield fluorescence microscope equipped with an incubation chamber. Only spheres that remained attached during the experiment were used for quantification. Mesothelial clearance was quantified as previously described[42,43].

Protein extraction and western blot analysis. Cells were lysed in RIPA lysis buffer (150 mM NaCl, 1.0% IGEPAL CA-630, 0.5% sodium deoxycholate, 0.1 SDS and

50 mM Tris (pH 8.0), with protease and phosphatase inhibitors) on ice for 30 min. Phosphatase and protease inhibitors added to the RIPA buffer (Sigma–Aldrich) were purchased as PhosSTOP and complete EDTA-free mini tablets, respectively (Roche). Western blots were performed as described[44] using the indicated antibodies: phospho-Tyr705 STAT3 (9131; Cell Signaling Technology), STAT3 antibody (sc-482; Santa Cruz Biotechnology) and tubulin (T5168; Sigma–Aldrich).

Luciferase assay. Heya8 cells were transfected with the STAT3-responsive luciferase reporter M67-luc (provided by J. Bromberg at the Memorial Sloan Kettering Cancer Center) and renilla luciferase (Promega) using lipofectamine 2000 (ref. [44]). Cells were pretreated with 1 µM JSI-124 for 1 h, then stimulated with 10 ng ml^{-1} oncostatin M (Peprotech) for 6 h. Luciferase activity was measured using a dual-luciferase kit (Promega) on a Luminoskan luminometer. Firefly luciferase activity was normalized to renilla and expressed relative to media controls.

Immunofluorescence. Formalin-fixed, paraffin-embedded tissues were cut at a thickness of 5 µm and mounted on glass slides. Direct immunofluorescence was performed as previously described[45] using the following antibodies: anti-HLA-DPB1-Alexa 647 (Abcam; clone EPR11226, 1:50) and anti-Pan-Cytokeratin-eFluor 570 (Thermo Fisher Scientific; AE1/AE3; 1:100). Images were acquired on a CyteFinder slide-scanning fluorescence microscope (RareCyte) using a 10× objective.

PDX model experiments. HGSOC PDX models derived from patients with different treatment histories were selected for implantation: DF20 (*BRCA1/2* wild type; treatment naive; clinically platinum sensitive); DF101 (*BRCA1* mutant; two lines of previous therapy; clinically platinum resistant); and DF68 (*BRCA1* mutant; six lines of previous therapy; clinically platinum resistant)[28]. For all of the experiments, we used NOD-SCID IL2Rγ^{null} mice (NSG; The Jackson Laboratory). For the carboplatin treatment study, to facilitate detecting minimal residual disease, we used a subcutaneous model instead of an intraperitoneal model.

Frozen stocks of tumor cells were briefly thawed, and 5×10^6 cells were injected subcutaneously into the flanks of NOD-SCID IL2Rγ^{null} mice (NSG; The Jackson Laboratory). After tumors were established (150–300 mm^3), animals were divided into two groups per model: vehicle ($n=5$) and carboplatin ($n=30$). Animals were treated with DMSO or with intraperitoneal carboplatin at 70 mg kg^{-1} weekly for three total doses. Mice were monitored by weight, clinical appearance and tumor burden (as determined by measurements using calipers and bioluminescence imaging (BLI)). For BLI imaging, the mice were anesthetized and imaged every 1–2 weeks. Vehicle-treated mice were harvested based on predefined criteria: 40% weight gain, 20% weight loss, ascites, or for humane reasons. Carboplatin-treated mice for the minimal residual disease group were harvested at the nadir of BLI signal and size. For the remaining carboplatin-treated mice, we continued weekly to biweekly BLI monitoring and harvested them at the end point using the same criteria as for the vehicle mice. For the minimal residual disease cohort, the entirety of the tumor was harvested for scRNA-seq. For the remaining carboplatin cohort, at the final harvest, the majority of the tumor was harvested for scRNA-seq with one fragment added to 10% neutral buffered formalin and one fragment snap frozen. Solid organs were also placed in formalin. Tumors and tissues were disaggregated as previously described[9]. Tumor cells expressing mCherry were isolated and flow-sorted into 96-well plates as described above, then subjected to plate-based scRNA-seq and analyzed in a pooled fashion.

For the JSI-124 treatment, PDX model DF20 was selected and 5×10^6 tumor cells were injected into two cohorts of mice: one subcutaneously to induce tumors; and one intraperitoneally to induce ascites ($n=5$ per group). For the first experiment (tumor formation), at 7 d post-injection of the tumor cells, the animals were treated with DMSO versus intraperitoneal JSI-124 at 1 mg kg^{-1} daily for 14 d. For the second experiment (established tumors), tumors were allowed to grow for 3 weeks after cell injection, then DMSO versus intraperitoneal JSI-124 dosing proceeded daily for 14 d. In each experiment, animals were monitored by BLI weekly and killed at the study end point at day 16.

Plate-based scRNA-seq data processing. Expression levels were quantified as $E_{i,j}=\log_2\left[\mathrm{TPM}_{i,j}/10+1\right]$, where $\mathrm{TPM}_{i,j}$ refers to transcripts per million for gene i in cell j, as calculated by RSEM for Smart-seq2 samples[46]. TPM values were divided by ten since we estimate the complexity of single-cell libraries to be about 100,000 transcripts and would like to avoid counting each transcript around ten times. This would be the case with TPM, which may inflate the difference between the expression level of a gene in cells in which the gene is detected and those in which it is not detected. This modification has a minimal influence on the expression values, but decreases the difference between the expression values of undetected genes (that is, zero) and that of detected genes (data not shown), thereby reducing the impact of dropouts on downstream analysis.

For each cell, we quantified two quality measures:

1. The number of genes for which at least one read was mapped, which is indicative of library complexity; and
2. The average expression level (E) of a curated list of housekeeping genes, which is meant to verify that genes expected to be expressed highly (regardless of cell type) are indeed detected as highly expressed.

Scatterplot analyses of all profiled cells separated low- and high-quality cells based on these two measures (data not shown), and we therefore conservatively excluded all cells with either fewer than 2,000 detected genes or an average housekeeping expression level (E) below 2.5, as was done in previous studies[9,47]. In each sample, we further excluded cells with ad-hoc thresholds in case there was a subset of cells with fewer detected genes that appeared to be of low quality by manual inspection. For cells passing these quality controls, the median number of detected genes was 7,892.

We used the remaining cells ($k=1{,}297$ for human samples and $k=795$ for mouse samples) to identify genes that are expressed at sufficient levels by calculating the aggregate expression of each gene i across the k cells, as $E_a(i)=\log_2\left[\mathrm{average}(\mathrm{TPM}_i)_{1,\ldots,k}+1\right]$, and excluded genes with $E_a<4$. For the remaining cells and genes, we defined relative expression by centering the expression levels, $E_{r_{i,j}}=E_{i,j}-\mathrm{average}(E_i)_{1,\ldots,k}$. The relative expression levels, across the remaining subset of cells and genes, were used for downstream analysis.

Droplet-based scRNA-seq data processing. The droplet-based data processing followed similar lines to that of the plate-based data, with the necessary changes to accommodate the change in platform:

1. TPM values were obtained from CellRanger.
2. Threshold values for the number of detected genes were modified, to accommodate for the lower detection rate of the droplet-based platform. The minimum number of detected genes was set to 1,000.
3. In addition, the droplet-based platform also enabled quantification of the number of transcripts (that is, unique molecular identifiers); therefore, we used a second filtering parameter of at least 4,000 transcripts. We did not use a threshold for housekeeping genes.
4. Genes were chosen for downstream analyses if they were detected with more than five transcripts by more than five cells.

Dimensionality reduction and clustering. Following the initial processing steps described above, we clustered the cells using t-stochastic neighborhood embedding (t-SNE; with a perplexity of 30 and default parameters of MATLAB's tsne function) followed by density clustering using DBscan (with the parameters epsilon=5 and min-points=10). In the case of smart-seq2 clusters, cluster 1 (which was dominated by cells of patient 8) was also assigned several outlier cells from patients 9 and 10, which were manually excluded from the downstream analysis. Clusters were annotated based on the expression of marker genes (as described above) and based on the top 30 most upregulated genes in each cluster (as defined by the fold-change between the average expression in the corresponding cluster compared with the average expression in all other clusters) (Figs. 1d and 2c). The malignant cell clusters were further supported by CNAs, which were estimated as described previously[9,47].

Expression programs of intra-tumoral heterogeneity. For each of five patients and each of the three PDX models for which we had profiles of >100 malignant cells, we used NMF to identify six to nine expression modules of genes coherently co-varying across the cells within each tumor separately. For this purpose, we used NMF (as implemented by the MATLAB nnmf function, with the number of factors set to ten) to identify variable expression programs. NMF was applied to the relative expression values (E_r) by transforming all negative values to zero. Notably, undetected genes included many drop-out events (genes that are expressed but are not detected in particular cells due to the incomplete transcriptome coverage), which introduced challenges for the normalization of scRNA-seq; since NMF avoids the exact normalized values of undetected genes (as they are all zero), it may be beneficial in analysis of scRNA-seq (data not shown). We retained only programs for which the standard deviation in cell scores within the respective tumor was larger than 0.8, which resulted in a total of 35 programs across the five human samples and 24 across the mouse models. The programs were compared by hierarchical clustering, using the number of overlapping genes (among the 50 top-scoring genes of each program) as a similarity metric. Five clusters of programs (two cell cycle and three inflammatory programs) were identified in the human samples based on a minimum overlap of ten genes between programs, and used to define meta-signatures. For each cluster, NMF gene scores were $\log_2$-transformed and then averaged across the programs in the cluster, genes were ranked by their average scores, and the top 30 genes were defined as the meta-signature.

To evaluate whether similar programs of intra-tumor heterogeneity recurred in the test dataset, we defined a small set of n core genes for each meta-signature, consisting of those genes that were identified in multiple tumors and/or were established as related to the program's inferred function. We then examined whether there was an enrichment of cells in which a large number of those genes were detected as expressed. We counted the number of cells in which the expression of X of those genes was detected, for $X=[1\ldots n]$. To assess the significance of the observed counts, we repeated the analysis 10,000 times with other sets of n genes referred to as control gene sets. Each control gene set was chosen such that it had a similar distribution of expression levels to that of the signature's core genes. To that end, we first partitioned all analyzed genes into 50 bins based on their average expression across all cancer cells. Next, we defined each

control gene set by randomly sampling from each bin the same number of genes that were in that bin among the signature's core genes. The fraction of simulations (out of 10,000) in which an equal number of the core signature genes were detected as expressed was used to define the *P* value of observed counts.

TCGA subtype scores and purity estimate. Bulk RNA-seq data of samples, as well as NMF clustering and differential expression analysis were downloaded from the Broad Institute Firehose website (https://gdac.broadinstitute.org/), along with additional tumor and clinical annotations. Classification of tumors to predefined molecular subtypes was done based on the NMF clustering with four factors, and the average expression of the top 100 differentially expressed genes for each cluster was defined as the subtype signatures, for which single-cell clusters were scored. Purity data was defined by ABSOLUTE[39].

Reporting Summary. Further information on research design is available in the Nature Research Reporting Summary linked to this article.

Data availability

Processed data are available from the Gene Expression Omnibus (GSE146026) and raw data are available via the Broad Institute Data Use Oversight System (https://duos.broadinstitute.org/#/home). Detailed instructions on establishing a Data Use Oversight System account can be found at https://duos.broadinstitute.org/#/home. Source data for Extended Data Fig. 8 are provided with the paper.

Code availability

Specific code will be made available upon request (without restrictions) to itay.tirosh@weizmann.ac.il. Code for inference of CNAs is available at https://github.com/broadinstitute/inferCNV.

References

40. Rotem, A. et al. Alternative to the soft-agar assay that permits high-throughput drug and genetic screens for cellular transformation. *Proc. Natl Acad. Sci. USA* **112**, 5708–5713 (2015).
41. Gazdar, A. F. & Oie, H. K. Re: growth of cell lines and clinical specimens of human non-small cell lung cancer in a serum-free defined medium. *Cancer Res.* **46**, 6011–6012 (1986).
42. Davidowitz, R. A. et al. Mesenchymal gene program-expressing ovarian cancer spheroids exhibit enhanced mesothelial clearance. *J. Clin. Invest.* **124**, 2611–2625 (2014).
43. Iwanicki, M. P. et al. Mutant p53 regulates ovarian cancer transformed phenotypes through autocrine matrix deposition. *JCI Insight* **1**, e86829 (2016).
44. Nelson, E. A. et al. Nifuroxazide inhibits survival of multiple myeloma cells by directly inhibiting STAT3. *Blood* **112**, 5095–5102 (2008).
45. Lin, J.-R. et al. Highly multiplexed immunofluorescence imaging of human tissues and tumors using t-CyCIF and conventional optical microscopes. *eLife* **7**, e31657 (2018).
46. Li, B. & Dewey, C. N. RSEM: accurate transcript quantification from RNA-Seq data with or without a reference genome. *BMC Bioinformatics* **12**, 323 (2011).
47. Patel, A. P. et al. Single-cell RNA-seq highlights intratumoral heterogeneity in primary glioblastoma. *Science* **344**, 1396–1401 (2014).

Acknowledgements

We thank the patients and their families. We also thank: L. MacDonald, A. McKelvey, J. Gelissen, J. Jacob, L. Frackiewicz, L. Dellostritto, K. Helvie and N. Straub from the Division of Gynecologic Oncology and the Center for Cancer Genomics at the Dana-Farber Cancer Institute for coordinating the clinical samples; members of the Belfer Center for Applied Cancer Science at the Dana-Farber Cancer Institute (particularly S. Palakurthi and P. Kirschmeier) for assistance with the PDX experiments; Jennifer Guerriero for helpful discussions; and L. Gaffney for help with the artwork. This work was supported by a Marsha Rivkin Scientific Scholar Award (to B.I. and E.H.S.), a Susan F. Smith Center for Women's Cancers Cancer Research Award (to B.I. and E.H.S.), the Wong Family Award for Translational Cancer Research (to B.I.), the Ludwig Center for Cancer Research at Harvard (to B.I.) and at MIT (to A.Regev), the Burroughs Wellcome Fund Career Award for Medical Scientists (to B.I.), the Dana-Farber Cancer Institute Claudia Adams Barr Program for Innovative Cancer Research (to B.I.), K08CA222663 from the National Cancer Institute (to B.I.), the Israel Cancer Research Fund (to I.T.), the STARR Cancer Consortium (to I.T. and A.Regev), the Human Frontier Science Program (to I.T.), the Mexican Friends New Generation (to I.T.), the Benoziyo Endowment Fund for the Advancement of Science (to I.T.), grant U54CA225088 from the National Cancer Institute (to P.K.S. and B.I.), the Koch Institute Support (core) grant P30CA14051 from the National Cancer Institute (to A.Regev), grant R33-CA202820 (to A.Regev and A.Rotem) and the Klarman Cell Observatory (A.Regev). A.Regev is an investigator of the Howard Hughes Medical Institute.

Author contributions

B.I., I.T., E.H.S., A.Rotem and A.Regev conceived of and designed the overall study. E.H.S., P.K., J.F.L. and U.M. provided samples and clinical annotation and reviewed the clinical data. C.B.M.P., M.S., J.W., L.J.-A., O.A., O.R.-R. and A.Rotem coordinated the data acquisition for HTAPP specimens. B.I., I.W., M.S.C., C.R., R.L., M.-J.S., P.S., J.C.M., T.J.B., M.R., S.V. O.R.-R., L.A.G., B.E.J. and A.Rotem coordinated and performed the sample acquisition and processing. B.I., S.V., A.Rotem and O.R.-R. oversaw sample processing. B.I., I.T., E.H.S., S.V., O.R.-R. and A.Rotem oversaw sample sequencing. I.T., B.I., E.H.S. I.A. and A.Regev performed and interpreted the computational analyses. B.I., E.H.S. and A.Rotem designed and oversaw the in vitro experiments. B.I., I.W., R.L., M.I., S.R.W., C.M., J.C.M. and A.Rotem performed and analyzed the in vitro experiments. B.I., S.M., P.K.S. and J.L. performed the IF experiments. B.I., E.H.S. and A.Rotem oversaw the in vivo experiments. B.I., I.T., E.H.S., A.Rotem and A.Regev interpreted the data. B.I., I.T., E.H.S., A.Rotem and A.Regev wrote the manuscript. All authors reviewed and approved the final manuscript.

Competing interests

B.I. is a consultant for Merck and Volastra Therapeutics. L.A.G. is an employee of Genentech. L.A.G. was previously an employee of Eli Lilly. L.A.G. was a paid consultant for Novartis, Foundation Medicine and Boehringer Ingelheim, held equity in Foundation Medicine and was a recipient of a grant from Novartis. P.K.S. is a member of the SAB or Board of Directors and holds equity in Applied Biomath, Glencoe Software and RareCyte. A.Rotem is a consultant to eGenesis, a member of the SAB in NucleAI and an holds equity in Celsius. A.Regev is a SAB member of Thermo Fisher Scientific, Neogene Therapeutics, Asimov and Syros Pharmaceuticals, a cofounder of and equity holder in Celsius Therapeutics, and an equity holder in Immunitas Therapeutics. B.I., I.T., E.H.S., L.A.G., O.R.-R., A.Rotem and A.Regev have filed a provisional patent for the use of JSI-124 for the treatment of ovarian cancer. The other authors have no conflicts of interest to declare.

Additional information

Extended data is available for this paper at https://doi.org/10.1038/s41591-020-0926-0.

Supplementary information is available for this paper at https://doi.org/10.1038/s41591-020-0926-0.

Correspondence and requests for materials should be addressed to A.R.

Peer review information Saheli Sadanand was the primary editor on this article and managed its editorial process and peer review in collaboration with the rest of the editorial team.

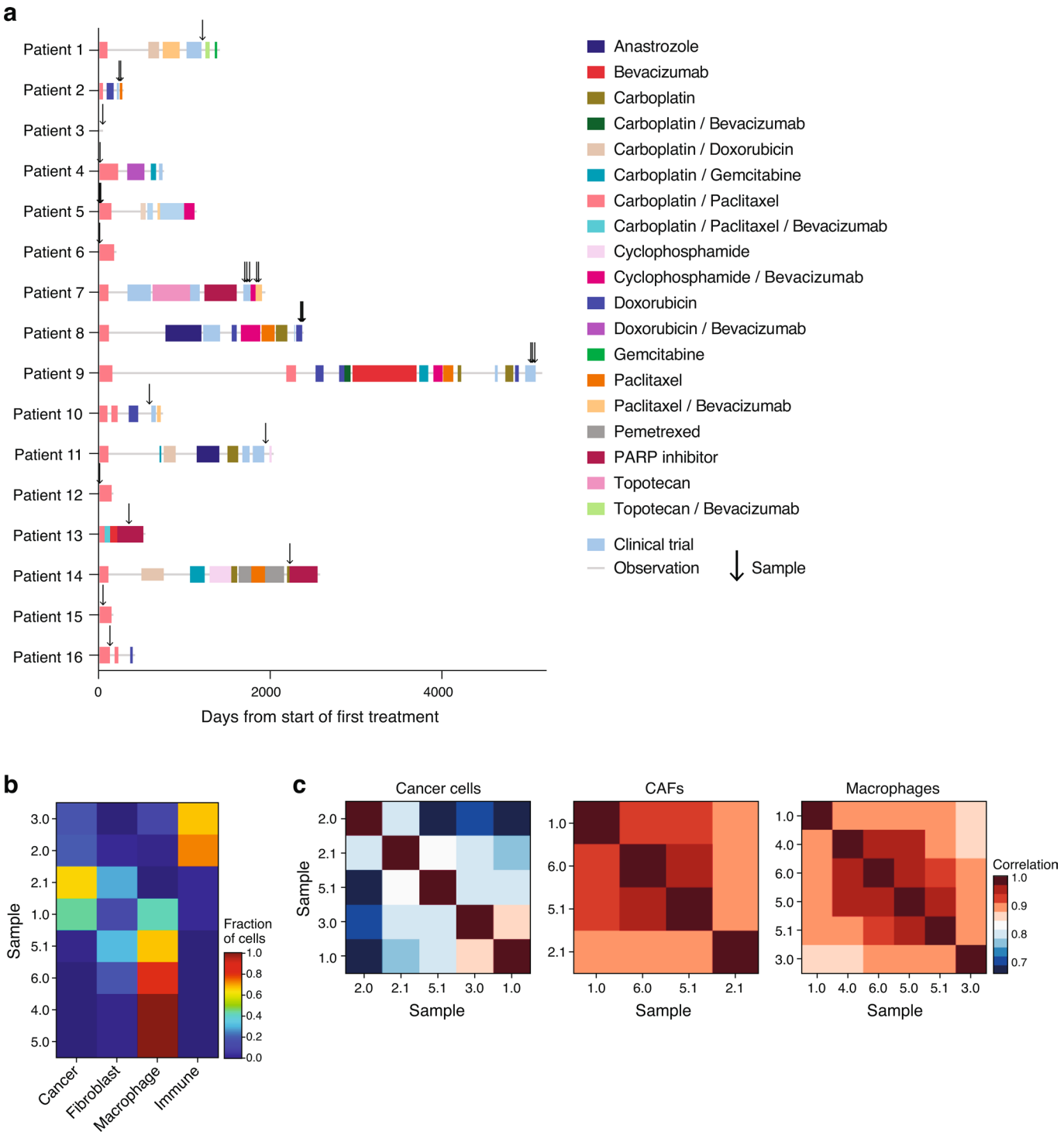

Extended Data Fig. 1 | Patient and sample characteristics. a, Timing (x axis, days) of therapies (color blocks) and sample collection (arrows) in each patient (y axis). **b**, Cell type composition does not group samples by treatment history. Proportion (color bar) of the four major cell types (columns) in each of the ascites samples (rows) profiled by droplet-based scRNA-seq. **c**, Cell intrinsic profiles do not group samples by treatment history. Pearson correlation coefficient (color bar) between the mean profiles of cancer cells (left), CAF (middle) or macrophages (right) of each pair of samples (rows, columns) profiled by droplet-based scRNA-seq and having at least 20 cells in each type.

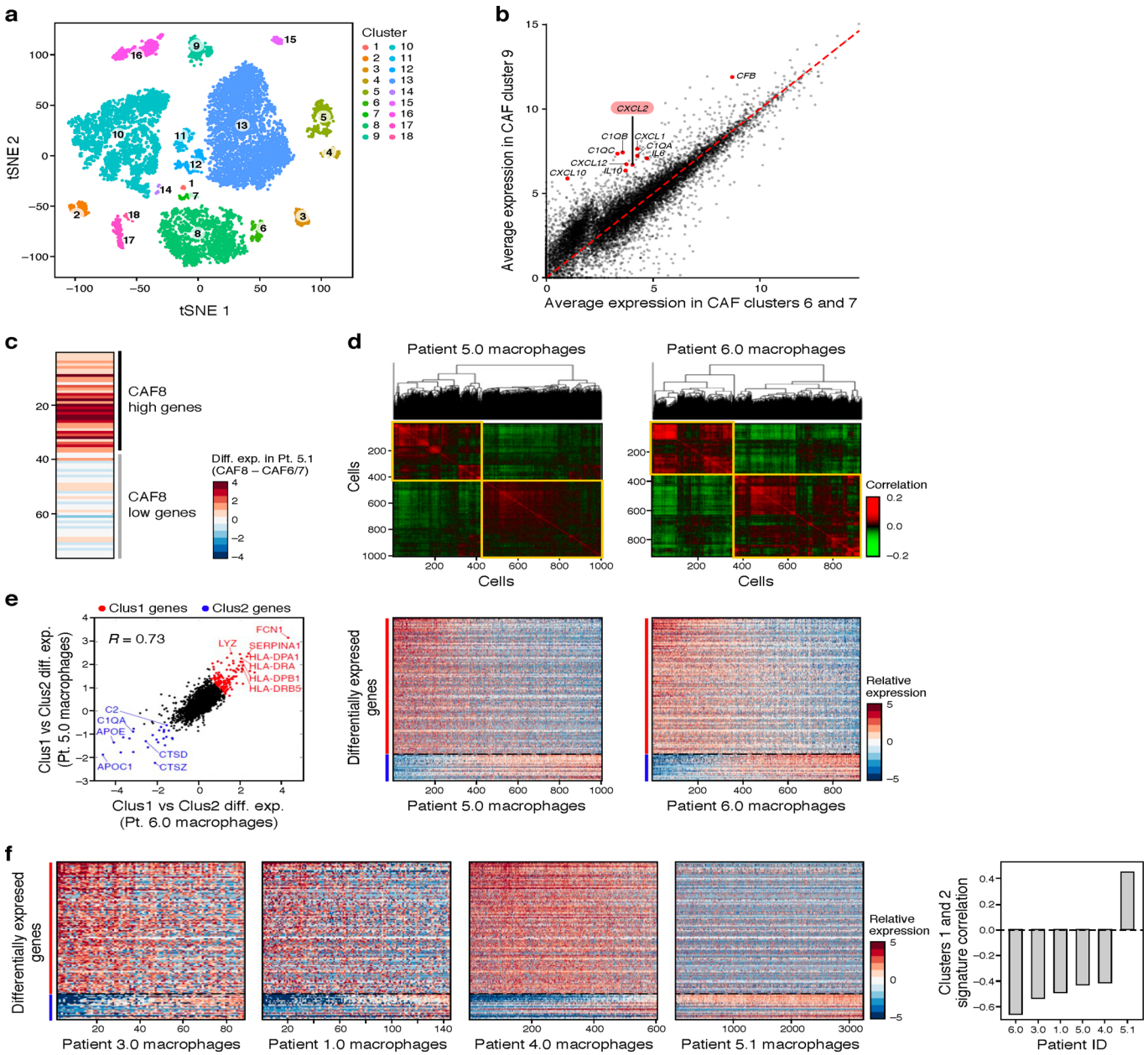

Extended Data Fig. 2 | Clustering and characterization of malignant and non-malignant cell clusters in patient ascites by droplet scRNA-seq. a, t-stochastic neighborhood embedding (tSNE) of 9,609 droplet-based scRNA-seq profiles from 8 samples (as in Fig. 1b), colored by unsupervised cluster assignment. **b**, Cluster 9 is an inflammatory subset of CAFs. Comparison of the average expression (log2(TPM+1)) of each gene in CAF cluster 9 (y axis) vs. CAF clusters 6 and 7 (x axis). Red: immunomodulatory genes. **c**, CAF diversity observed within a single sample. Differential expression (log2(TPM+1)) between CAF8 and CAF6/7 cells in patient 5.1 only of the top up- and down- regulated genes from (**b**). (**d**-**f**) Two distinct macrophage programs. **d**, Hierarchical clustering of macrophages (rows, columns) from cluster 10 from either Patient 5.0 (left) or Patient 6 (right). Shown are the Pearson correlation coefficients (color bar) between expression profiles of macrophages, ordered by the clustering. Yellow lines highlight the separation into two main clusters. **e**, Left: Differential expression (log2(fold change)) for each gene (dot) between the two clusters identified in (**d**) for Patient 6 (x axis) or patient 5 (y axis), demonstrating high consistency. Top left corner: Pearson's r. Genes significantly differentially up or down regulated in both patients are marked in red and blue, respectively. Middle and Right: Expression levels (color bar, log2(fold change)) of the highlighted differentially expressed genes from the left panel (rows) across macrophages from Patient 5 (middle) and Patient 6 (right) sorted by the hierarchical clustering of (**d**). (**f**) As in (**e**) for each other samples tested. Right panel: correlation between the average expression of cluster 1 and cluster 2 genes across cells from each of the samples tested.

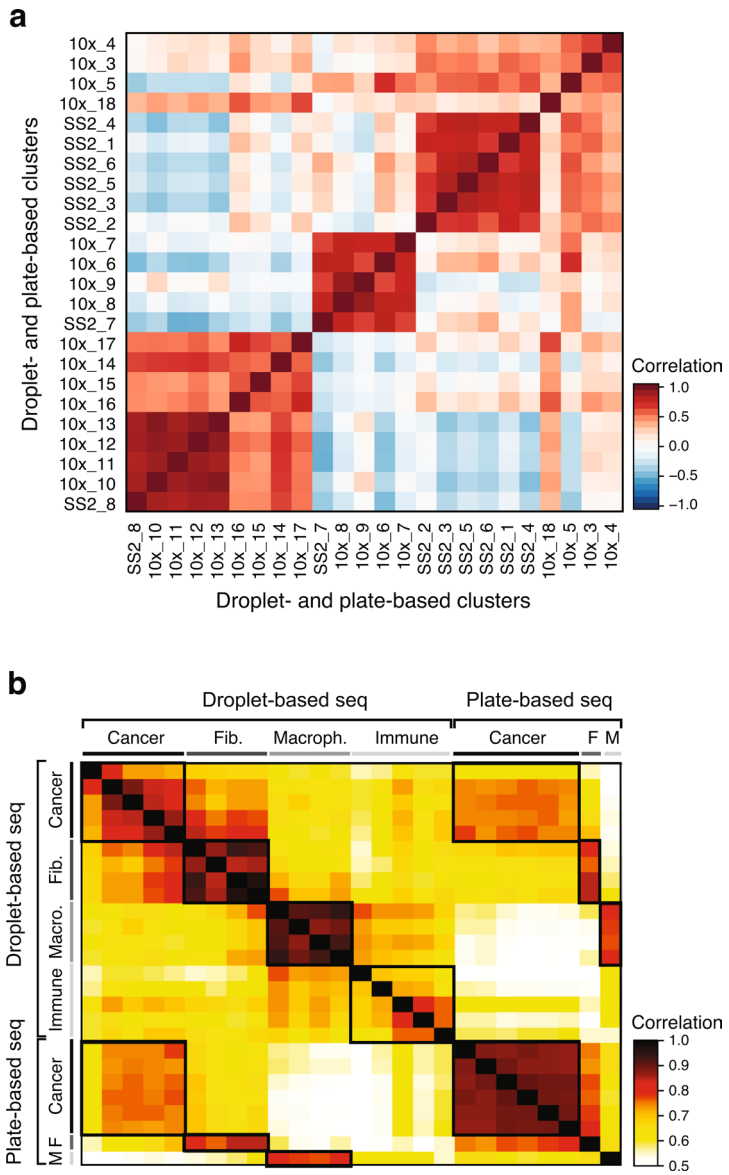

Extended Data Fig. 3 | Consistent clusters among droplet and plate based scRNA-seq. a, Pearson correlation coefficient (color bar) between the average expression profiles of 302 cluster marker genes in cells in clusters defined from either droplet-based or plate-based scRNA-seq (rows, columns; ordered by hierarchical clustering). **b**, Pearson correlation coefficient of the mean profile of cell type specific clusters comparing droplet based and plate-based scRNA-seq.

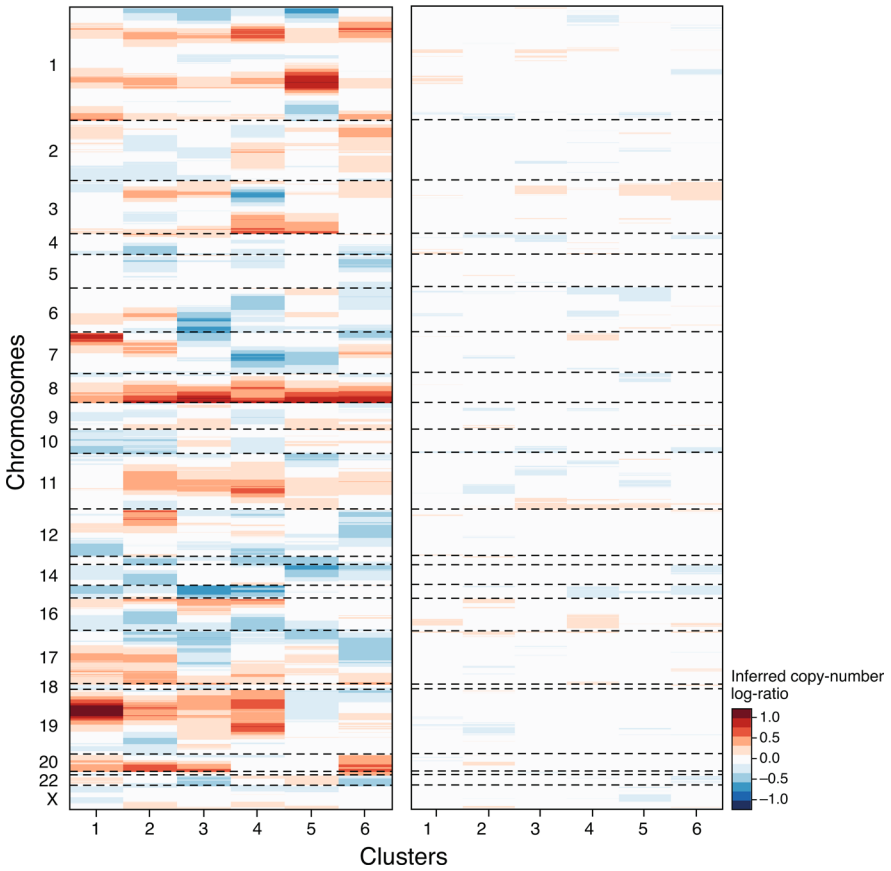

Extended Data Fig. 4 | Inferred CNA of single cells from plate based scRNA-seq profiles. Average relative copy number (color bar) in each chromosomal position (y axis) based on the average expression of the 100 genes surrounding that position (ref. [9]) in each cell in the malignant cell clusters 1-6 (x axis), compared to non-cancer clusters used as a reference, when using the original data (left) or when randomly ordering the genes across the genome and repeating the analysis (right), as control.

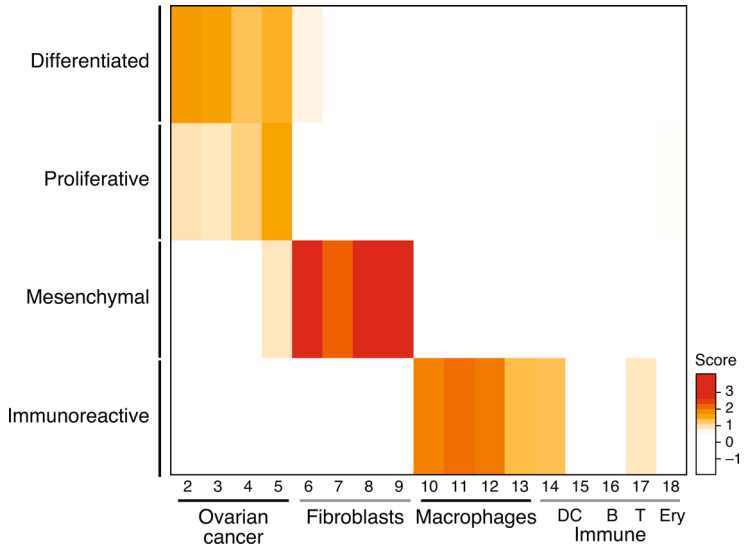

Extended Data Fig. 5 | Mesenchymal and immunoreactive TCGA subtypes reflect CAFs and macrophages by comparison to droplet based scRNA-seq profiles. Subtype score (color bar), based on average expression of subtype-specific genes (Methods) of each cluster from the droplet-based scRNA-seq dataset (rows) for each of four TCGA subtypes (column). Only clusters with > 10 cells are represented in this figure.

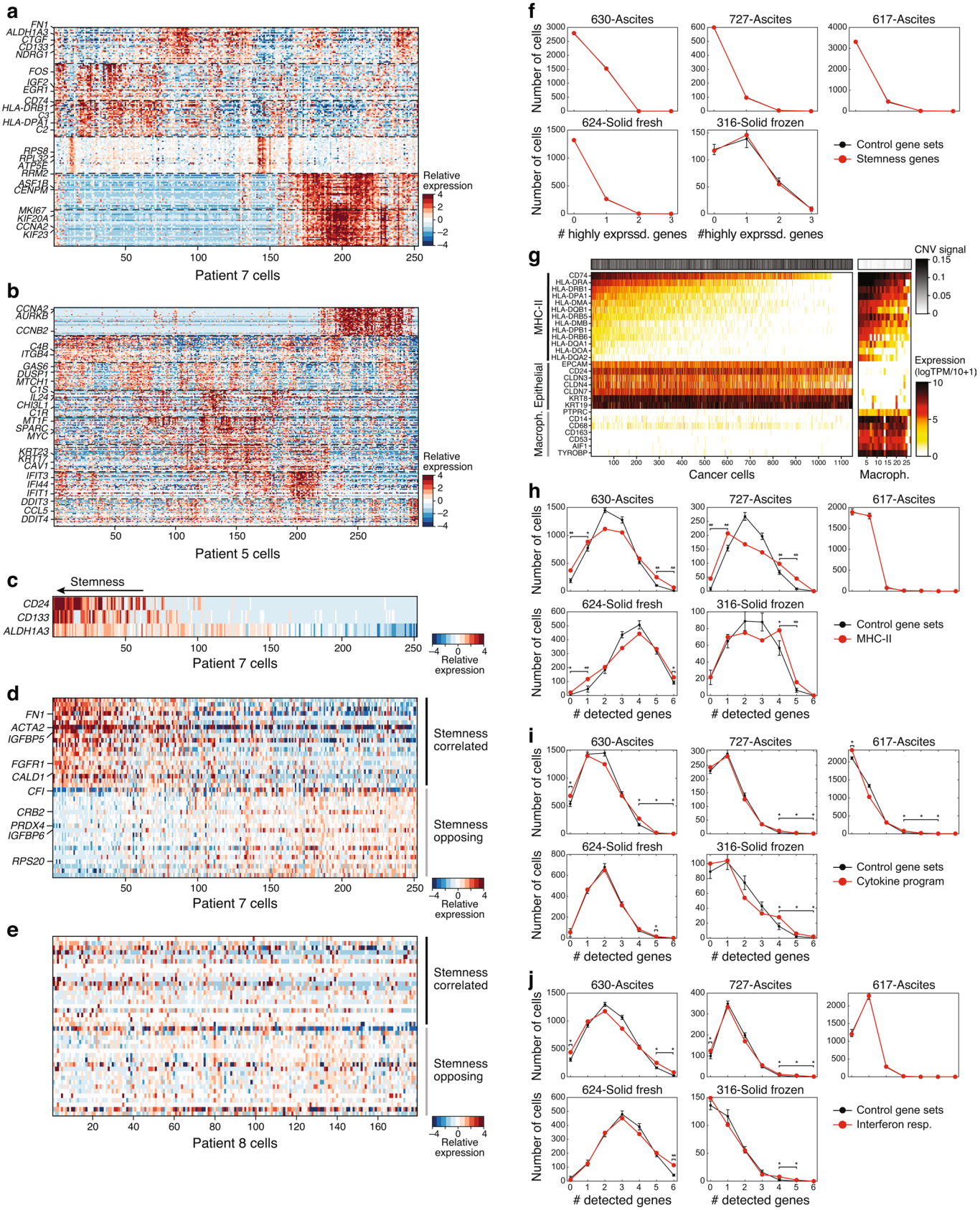

Extended Data Fig. 6 | See next page for caption.

Extended Data Fig. 6 | A putative stemness program in Patient 7 modules. a,**b**, Intra-tumoral expression modules in patients 7 and 5. Relative expression (color bar, Methods) of the top 30 module-specific genes (rows) in each module (ordered by module, dashed vertical lines), as defined by NMF (Methods) across all cancer cells (columns; ordered by hierarchical clustering) from patients 7 (**a**), or 5 (**b**, same as Fig. 3a–c). Selected genes are annotated. **c**, Co-variation of stemness related genes in patient 7. Relative expression of three putative stemness markers (rows) in cells from patient 7, rank ordered by the cell's average expression of the three markers. **d**,**e**, Stemness related co-varying module present in patient 7 but not patient 8. Relative expression of the stemness score of patient 7 (top 20 genes (row) positively (top) or negatively (bottom)) correlated with the average expression of the three stemness genes in (**c**) in either cells from patient 7 (**d**) or patient 8 cells (**e**), with cells ordered by their average expression of the putative stemness score. (**f**) Stemness program is not detected in other ascites and primary tumor samples from our test cohort. Number of cells (y axis) expressing increasing numbers (x axis) of genes defining the stemness program from Patient 7 (*CD24*, *CD133* (*PROM1*) and *ALDH1A3*) in patient cohort 3 (red) or expressing control genes with similar expression pattern in 10,000 simulations (**g**) Identification of cells expressing MHC Class II as cancer cells. Expression (color bar, log(TP100K + 1)) of MHC Class II program, epithelial (cancer cell) markers, and macrophage markers (rows) in cancer cells (defined by marker expression and CNA) and macrophages (columns). Top panel: CNA signal, defined as the square of the inferred copy-number log-ratios, averaged across all genes. (**h**–**j**) MHC-II, cytokine and interferon programs are detected in other ascites and primary tumor samples from our test cohort. As in (f) for the three major immune programs defined as (**h**) MHC Class II (core genes (*CD74, HLA-DRA, HLA-DRB1, HLA-DRB5, HLA-DMA, HLA-DPA1*), (**i**) cytokines (core genes *TNF, CXCL8, IL32, ICAM1, CCL2, CCL20, NFKBIA*); and (j) interferon (IFN) program (core genes *IFI6, IFI44, IFIT1, IFIT3, ISG15, MX1*). Error bars: SD, *=$p < 0.05$, **=$p < 0.001$; empirical p-value is the fraction of simulations in which an equal number of stemness-program genes are detected as expressed.

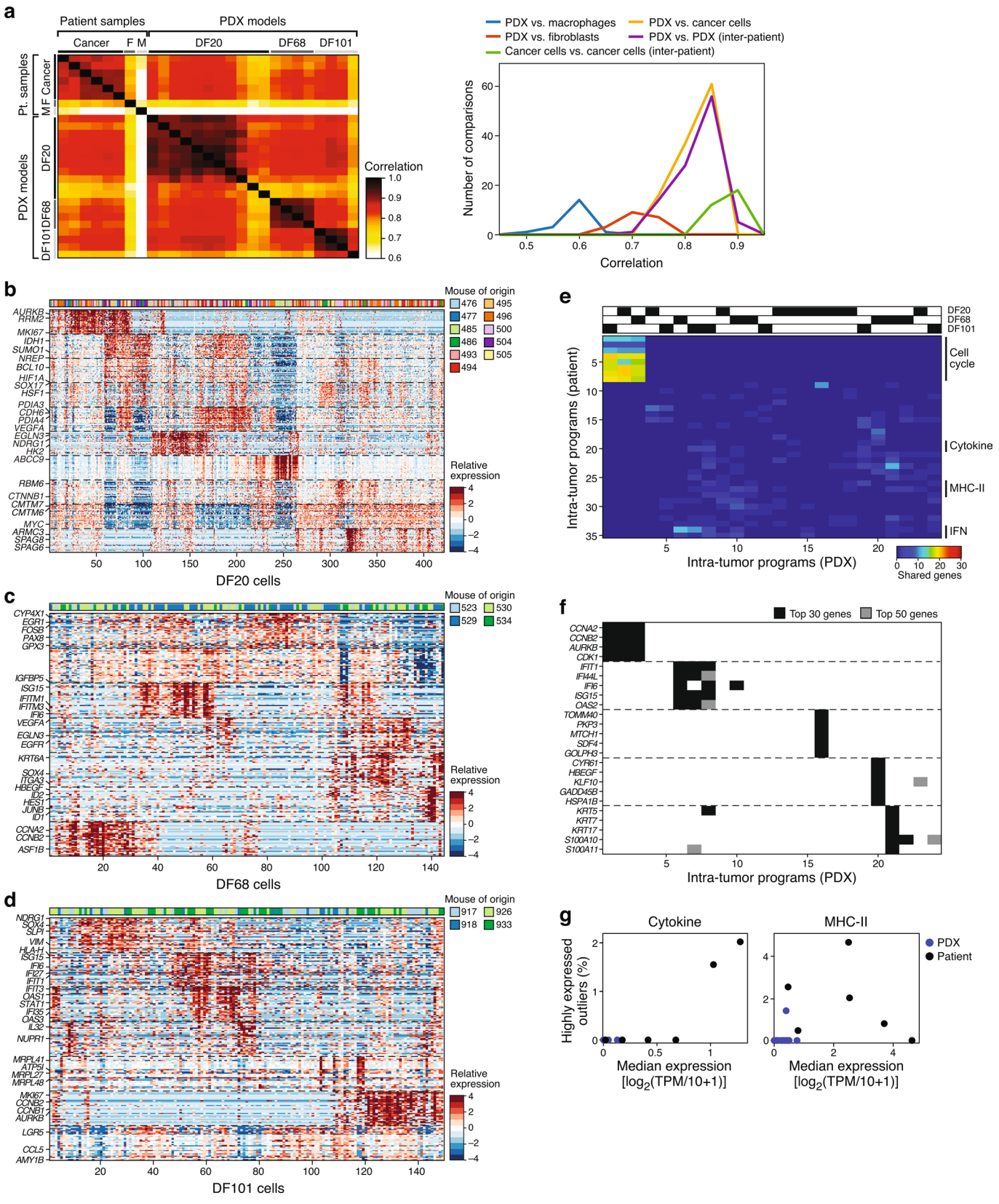

Extended Data Fig. 7 | See next page for caption.

Extended Data Fig. 7 | Some programs in malignant cells recur between patient ascites and PDX. a, Congruent cancer cell profiles between patient and PDX cells. Left: Pearson correlation coefficient (color bar) between mean profiles (rows, columns) among major cell types discovered by plate-based scRNA-seq (cancer cells, macrophages and CAFs) in patient samples and three patient-derived xenograft models (DF20, DF68 and DF101). Right: Distribution of Pearson correlation coefficient (x axis) between different subsets. n = 27 (8 patient samples and 19 PDX samples). **b**–**d**, Intra-tumoral expression modules. Relative expression (color bar, Methods) of the top 30 module-specific genes (rows) in each module (ordered by module, dashed horizontal lines), as defined by NMF (Methods) across all cancer cells (columns; ordered by hierarchical clustering) from PDX models DF20 (**b**), DF68 (**c**), and DF101 (**d**). Selected genes are annotated. Top bar (**b**, **c**): cell of origin from individual mice. **e**,**f**, Cell cycle and inflammatory/immune programs recur across PDX models. (**e**) Number of top genes (color bar) shared between pairs of patients (rows, ordered as in Fig. 3e) and PDX (columns; ordered by hierarchical clustering) modules. Top: origin of each PDX module. (f) Module membership in the top 30 (black) or 50 (grey) of selected genes (rows) from cell cycle (top), immune-related (middle), and other (bottom) modules across all modules (columns), ordered as in (**e**). All genes included were shared between a corresponding PDX module and patient ascites module. **g**, Cytokine and MHC-II programs are only identified in patient samples. Median expression (x axis) and % of outlier highly expressing cells (y axis; average log2(TPM + 1)>5 and more than 2 SD larger than the mean of all cells) of the cytokine (left) and MHC-II (right) programs in each patient (black) and PDX (blue) samples. N = 25 (6 patient samples and 19 PDX samples).

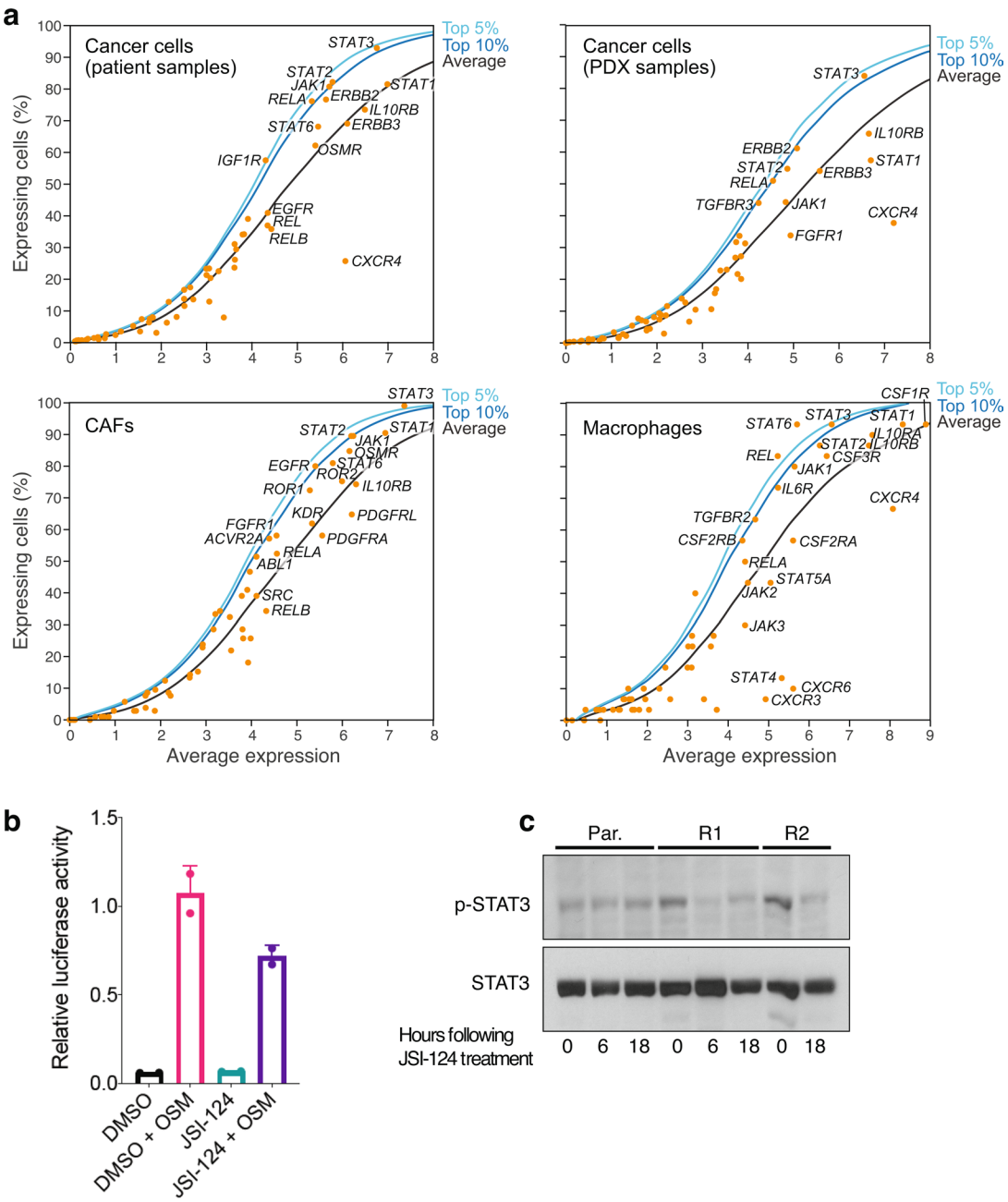

Extended Data Fig. 8 | Prominent expression of JAK-STAT pathway genes and on-target activity of JSI-124 against STAT3. a, Prominent expression of JAK-STAT pathway genes. Mean gene expression (x axis, log2(TPM + 1)) and percentage of expressing cells (y axis) across the entire cell's transcriptomes with highlighted signaling genes in patient cancer cells (top left), PDX models (top right), patient-derived CAFs (bottom left) and macrophages (bottom right). Black curve: LOWESS regression curve. Dark and light blue: top 5 and 10 percentiles calculated in a moving average of 200 genes. **b**, STAT3 activity induced by Oncostatin M. Relative (mean) luciferase activity (y axis) in Heya8 ovarian cancer cells transfected with a STAT3 responsive reporter that were stimulated with OSM to activate STAT3 for 6 h or untreated with either 1 h pre-treatment with JSI-124 (1 μM) or vehicle (x axis) for 1 h. $p = 0.09$, t test. Error bars: SD. **c**, JSI-124 treatment reduced pSTAT3. Cropped immunoblot (representative of duplicates; uncropped available in Source Data) of STAT3 and phosphorylated (p-)STAT3 from cells treated with 1μM JSI-124 for the indicated hours (bottom). Par=parental cell line, and R1 and R2 refer to two independently generated platinum-resistant cell lines.

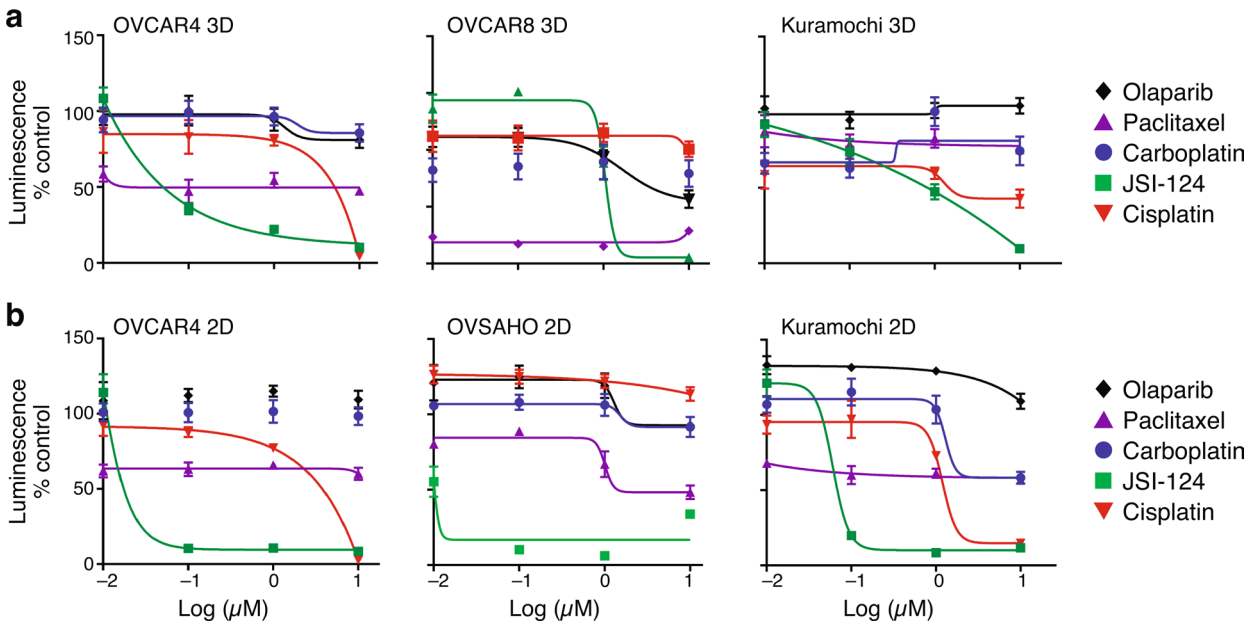

Extended Data Fig. 9 | Dose response of JSI-124 in 2D cultures or 3D spheroids. Relative (mean) viability (y axis, relative luminescence signal compared to DMSO control) of three ovarian cancer cell lines (labels, top) grown for 4 days in either ultra-low attachment conditions eliciting formation of spheroids **a**, or in 2D cultures in regular plastic culture surfaces **b**, and treated with JSI-124, carboplatin, paclitaxel, cisplatin or olaparib at indicated doses (x axis, log μM). Error bars: SD. n = 4. Representative of biological duplicates.

nature research

Corresponding author(s): Aviv Regev

Last updated by author(s): 5/1/2020

Reporting Summary

Nature Research wishes to improve the reproducibility of the work that we publish. This form provides structure for consistency and transparency in reporting. For further information on Nature Research policies, see our Editorial Policies and the Editorial Policy Checklist.

Statistics

For all statistical analyses, confirm that the following items are present in the figure legend, table legend, main text, or Methods section.

n/a	Confirmed
☐	☒ The exact sample size (*n*) for each experimental group/condition, given as a discrete number and unit of measurement
☐	☒ A statement on whether measurements were taken from distinct samples or whether the same sample was measured repeatedly
☐	☒ The statistical test(s) used AND whether they are one- or two-sided *Only common tests should be described solely by name; describe more complex techniques in the Methods section.*
☐	☒ A description of all covariates tested
☐	☒ A description of any assumptions or corrections, such as tests of normality and adjustment for multiple comparisons
☐	☒ A full description of the statistical parameters including central tendency (e.g. means) or other basic estimates (e.g. regression coefficient) AND variation (e.g. standard deviation) or associated estimates of uncertainty (e.g. confidence intervals)
☐	☒ For null hypothesis testing, the test statistic (e.g. *F*, *t*, *r*) with confidence intervals, effect sizes, degrees of freedom and *P* value noted *Give P values as exact values whenever suitable.*
☐	☒ For Bayesian analysis, information on the choice of priors and Markov chain Monte Carlo settings
☐	☒ For hierarchical and complex designs, identification of the appropriate level for tests and full reporting of outcomes
☐	☒ Estimates of effect sizes (e.g. Cohen's *d*, Pearson's *r*), indicating how they were calculated

Our web collection on statistics for biologists contains articles on many of the points above.

Software and code

Policy information about availability of computer code

Data collection	CellRanger (v3.0) for 10x Genomics data
Data analysis	Graphpad Prism version 8 was used for statistical assessment of in vitro and in vivo data. For single-cell RNA-sequencing analysis, the following software was used: custom scripts in MATLAB and R, as described further on the Methods. We used Microsoft Word for preparation of the Manuscript and Microsoft Excel for preparation of Tables.

For manuscripts utilizing custom algorithms or software that are central to the research but not yet described in published literature, software must be made available to editors and reviewers. We strongly encourage code deposition in a community repository (e.g. GitHub). See the Nature Research guidelines for submitting code & software for further information.

Data

Policy information about availability of data

All manuscripts must include a data availability statement. This statement should provide the following information, where applicable:

- Accession codes, unique identifiers, or web links for publicly available datasets
- A list of figures that have associated raw data
- A description of any restrictions on data availability

Processed Data is deposited and available in Gene Expression Omnibus (GSE146026)
Raw Data is also deposited on https://portals.broadinstitute.org/single_cell.
Readers can request access to raw data after registering here: https://duos.broadinstitute.org/#/home.
Additional, specific code will be made available without restrictions upon request to: itay.tirosh@weizmann.ac.il

Field-specific reporting

Please select the one below that is the best fit for your research. If you are not sure, read the appropriate sections before making your selection.

☒ Life sciences ☐ Behavioural & social sciences ☐ Ecological, evolutionary & environmental sciences

For a reference copy of the document with all sections, see nature.com/documents/nr-reporting-summary-flat.pdf

Life sciences study design

All studies must disclose on these points even when the disclosure is negative.

Sample size	No sample size calculation was necessary or performed. As seen in the analysis, all biological specimens available we used and included in the analysis, and biological conclusions, with appropriate discussion of potential limitations of sample size, could be made from available data.
Data exclusions	No data was excluded from the study.
Replication	Experiments were done in multiple replicates and produced comparable results. For human biological specimens, entire samples were used for processing, hence, no additional replicates were available.
Randomization	In mouse experiments, animals were randomized after initial injection of SC or IP tumor cells. Such concepts are irrelevant to the other in vitro and ex vivo experiments, because all known variables were controlled for in those settings.
Blinding	Blinding was not done because the compounds used for e.g. mouse experiments have a fluorescence, hence, blinding was not possible. Notably, injection and treatment of animals were done by a specialized mouse technician.

Reporting for specific materials, systems and methods

We require information from authors about some types of materials, experimental systems and methods used in many studies. Here, indicate whether each material, system or method listed is relevant to your study. If you are not sure if a list item applies to your research, read the appropriate section before selecting a response.

Materials & experimental systems

n/a	Involved in the study
☐	☒ Antibodies
☐	☒ Eukaryotic cell lines
☒	☐ Palaeontology and archaeology
☐	☒ Animals and other organisms
☐	☒ Human research participants
☐	☒ Clinical data
☒	☐ Dual use research of concern

Methods

n/a	Involved in the study
☒	☐ ChIP-seq
☒	☐ Flow cytometry
☒	☐ MRI-based neuroimaging

Antibodies

Antibodies used	STAT3 (Santa Cruz Biotech, sc-482, Polyclonal), p-STAT3 (CST, 9131, Polyclonal), Tubulin (Sigma, T5168, Clone B-5-1-2), HLA-DPB1-Alexa647 (Abcam, ab201347, Clone EPR11226, 1:50), Pan-Cytokeratin-eFluor570, (ThermoFisher, 41-9003-82, Clone AE1/AE3, 1:100), CD45-FITC (VWR, 304006, Clone HI30), EPCAM-PE (Miltenyi Biotec, 130-111-116, REA764), CD24-PE/Cy7 (BioLegend, 311119, Clone ML5).
Validation	All of the antibodies used in this study were validated for the use in human specimens by the manufacturers and for the respective methods used in this manuscript (see home pages of respective manufacturers using catalogue numbers provided above).

Eukaryotic cell lines

Policy information about cell lines

Cell line source(s)	OVACR4, OVACR8, OVASHO, TYKU and Kuramochi were obtained from the Cancer Cell Line Encyclopedia (Broad Institute) and patient cell lines were derived from specimens obtained at Dana-Farber Cancer Institute.
Authentication	Cell lines were authenticated by the Cancer Cell Line Encyclopedia (CCLE) platform at the Broad Institute. Short-term cultures were derived from unique patient specimens.
Mycoplasma contamination	Cell lines were tested for Mycoplasma and were not infected.

Commonly misidentified lines (See ICLAC register)	None used in this study.

Animals and other organisms

Policy information about studies involving animals; ARRIVE guidelines recommended for reporting animal research

Laboratory animals	8-10 weeks old, female, NOD-SCID IL2Rγnull mice (NSG, Jackson Laboratory)
Wild animals	This study did not involve wild animals.
Field-collected samples	This study did not involve field-collected samples.
Ethics oversight	The IRB of the Dana-Farber/Harvard Cancer Center approved the studies presented in this work.

Note that full information on the approval of the study protocol must also be provided in the manuscript.

Human research participants

Policy information about studies involving human research participants

Population characteristics	All patients involved in this study were females diagnosed with high-grade serous ovarian cancer. Samples were obtained before treatment was initiated and/or during therapy with platinum-based chemotherapy or other clinically used agents or in the context of a clinical trial, and at the time of drug resistance.
Recruitment	Patients were consented per IRB protocols of the DF/HCC. Patients who were consented and had sufficient amounts of ascites were included. There were no other criteria for selecting or excluding patients to this study.
Ethics oversight	The IRB of the Dana-Farber/Harvard Cancer Center approved the studies presented in this work.

Note that full information on the approval of the study protocol must also be provided in the manuscript.

Clinical data

Policy information about clinical studies

All manuscripts should comply with the ICMJE guidelines for publication of clinical research and a completed CONSORT checklist must be included with all submissions.

Clinical trial registration	These patients were not enrolled to clinical trials.
Study protocol	These patients were not enrolled to clinical trials.
Data collection	These patients were not enrolled in clinical trials, however, some clinical data was collected. The clinical annotation available in this manuscript was collected at Dana-Farber Cancer Institute by CRCs.
Outcomes	There were not primary or secondary endpoints collected.